

A Near-Infrared Survey of the Inner Galactic Plane for Wolf–Rayet Stars III. New Methods: Faintest WR Stars

G. Kanarek,¹ M. Shara,² J. Faherty,³ D. Zurek,² A. Moffat⁴

¹*Columbia University, 116th St & Broadway, New York, NY 10027*

²*American Museum of Natural History, 79th Street and Central Park West, New York, NY, 10024*

³*Department of Terrestrial Magnetism, Carnegie Institution of Washington, 5241 Broad Branch Road NW, Washington, DC 20015*

⁴*Département de Physique, Université de Montréal, CP 6128 Succ. C-V, Montréal, QC, H3C 3J7, Canada*

16 June 2015

ABSTRACT

A new method of image subtraction is applied to images from a J , K , and narrow-band imaging survey of 300 deg^2 of the plane of the Galaxy, searching for new Wolf–Rayet stars. Our survey spans 150° in Galactic longitude and reaches $b = \pm 1^\circ$ with respect to the Galactic plane. The survey has a useful limiting magnitude of $K = 15$ over most of the observed Galactic plane, and $K = 14$ (due to severe crowding) within a few degrees of the Galactic centre. The new image subtraction method described here (better than aperture or even point-spread-function photometry in very crowded fields) detected several thousand emission-line candidates. In 2011 and 2012 June and July, we spectroscopically followed up on 333 candidates with MDM–TIFKAM and IRTF–SPEX, discovering 89 emission-line sources. These include 49 Wolf–Rayet stars, 43 of them previously unidentified, including the most distant known Galactic WR stars, more than doubling the number on the far side of the Milky Way. We also demonstrate our survey’s ability to detect very faint PNe and other NIR emission objects.

Key words: stars: emission-line, Be – stars: Wolf–Rayet – Galaxy: stellar content – planetary nebulae: general – infrared: stars

1 INTRODUCTION

In the more than 140 years since their first identification (Wolf & Rayet 1867), Wolf–Rayet (WR) stars have remained one of the most interesting (and, at times, baffling) classes of stars. Their huge masses ($\geq 25\text{ M}_\odot$ for initial stellar mass) and short lifetimes (typically $\sim 3 \times 10^5$ years in the WR phase) make them excellent tracers of recent star formation, and their position in the stellar evolutionary chain is important to both stellar astrophysics and supernova theory. The intense stellar winds of WR stars add a significant amount of C and O, and some N, to the interstellar medium (ISM), and contribute a significant fraction of the ISM’s energy and momentum budget; they also produce characteristic emission lines which give astronomers a probe into the atmospheres of these very hot, evolved stars.

The most reliable method to date of WR detection has been to look for narrowband excess due to emission lines in the optical, particularly the strong He II 4686 Å line. However, probing the Milky Way using this technique is difficult beyond $\sim 3\text{ kpc}$ due to extreme dust extinction (~ 30 visual magnitudes across and through the centre of the Galaxy); in the near-infrared (NIR) only ~ 3 magnitudes of extinction occurs across the Galactic plane (see Shara et al. 1999, sec-

tion 7). Clearly the NIR is the wavelength range of choice for searching out the vast majority of WR stars in the Milky Way.

Over the last 5 years, advances in NIR selection techniques have led to the identification of more than 250 new WR stars, using a variety of methods. Two earlier papers in this series have focused on photometric techniques, and identified 112 new WR stars in the Galactic Plane (Shara et al. 2009, 2012, hereafter Paper I and Paper II, respectively). In addition, various colour-selection criteria in the near- and mid-infrared have been developed; see Hadfield et al. (2007), Mauerhan, Van Dyk, & Morris (2009), Mauerhan, Van Dyk, & Morris (2011), and Messineo et al. (2012) (as well as Faherty et al. (2014) for a discussion of the specific techniques used in this paper).

Simple models of the WR distribution in the Galaxy predict high concentrations near the Galactic centre (Paper I), where extremely crowded images cause usual photometric techniques to fail. However, using a new method of image subtraction, along with NIR and MIR colour-cuts we are able to significantly improve the selection criteria in the most crowded parts of the Galaxy; follow-up of candidates with this new technique produced 89 new emission-line sources in

the Galactic Plane, including 49 new Wolf–Rayet stars. In section 2 we briefly describe the imaging survey and data reduction pipeline. Spectrographic follow-up data reductions are described in section 3, and the new candidates are presented in section 4. The resulting overall distribution of all known WR stars is presented and discussed in section 5. We briefly summarize our conclusions in section 6.

2 SURVEY & DATA REDUCTION PIPELINE

This survey was previously described in Paper I. More than 88,000 exposures were taken of the Galactic plane on the CTIO 1.5-m telescope over approximately 200 nights during 2005–2006. The survey covers 1° above and below the Galactic plane, from longitudes -90° to 60° . The images are 35×35 arcmin², with 1.03 arcmin pixel⁻¹ plate scale, in four narrowband filters as well as the *J* and *K* bands. The narrowband filter set is described in Paper I, with the central wavelengths and FWHMs of the emission-line filters repeated in table 1. The justification for the narrowband filters is: WCs can be discriminated using the ratio of the C IV 2.081 μ m filter to a 2.112 μ m He I line, and WNs with the ratio between the He II 2.192 μ m filter and each of the 2.112 μ m line and the 2.169 μ m Br γ filters.

The images from this survey were completely re-reduced for the new image-differencing pipeline described in this paper. Super dome flats for each month were created by combining all dome flats in that month. The images were then divided by the master dome flats. A skyflat was created by median-combining the first dither positions from all the separate pointings. The skyflat was then scaled to match each image in the dither sequence and subtracted. Next, DAOPHOT (Stetson 1987) was used to find sources in each of seven dither positions for every field. The sources were matched using DAOMATCH and DAOMASTER, and finally the 7 dither positions were combined using MONTAGE2 (Stetson 1994).

World Coordinate System (WCS) astrometry for the images was computed by the ASTROMETRY.NET package (Lang et al. 2010), using *J* and *K* index files with sky-mark diameter ranges from 8 to 11 arcmin. The program was called with xy-lists obtained by the NASA IDL Astronomy Library’s version of DAOPHOT’s FIND procedure (Landsman 1993), using the 500 brightest stars in each image. After including SIP distortion coefficients, mean residuals less than 0.5 arcsec were found when compared to 2MASS sources (Skrutskie et al. 2006). Then, working on a field-by-field basis, we computed photometry using the IDL-DAOPHOT procedures SKY, FIND, and APER, and the positions output by these routines were matched among the images, to a precision of $\sim 1''$. Sources were then matched to 2MASS source lists in *J* and *K*, and a mean magnitude offset calculated to calibrate the photometry library to 2MASS.

Once WCS solutions and photometry had been obtained, we performed image differencing in wavelength-space, which provided a method to find rare emission-line sources from very crowded images. We generated a continuum image for each emission-line-centred narrowband image (ENB) by linearly interpolating between the two continuum narrowband (CNB) images in wavelength space; this interpolated image (INB) was then subtracted from the emis-

sion line image to produce the residual. Images were subdivided to allow modelling of the spatially-varying sky background by an array of intersecting planes. After removal of the background, stellar positions in each subdivision were matched between images and a translation/rotation warp was applied to spatially align subdivisions as accurately as possible. Higher-order warp solutions were not found to improve alignment significantly.

After warping the subdivisions to match, we scaled the global brightness between the ENB and INB images. Through trial and error we concluded that no single method of determining a scaling factor worked for all images (or even all subdivisions); thus, to remove outliers, five different scaling factors were determined for each subdivision, using different methods. The final scaling factor was chosen as the median value of all methods on all subdivisions. No PSF matching was performed, as (a) each image had a PSF which displayed large spatial variations, and (b) the blurring due to convolution was generally catastrophic to the resolution of the images.

Once the ENB and INB images were matched as closely as possible, the difference image was obtained. Figure 1 shows the C IV ENB image (left) and difference image (i.e. on-line intensity including continuum, minus interpolated and scaled off-line continuum-only intensity, right) for field 1093, a typical field which lies 24° from the Galactic Centre, and is relatively crowded, containing 6 previously known WR stars. The difference image in figure 1 demonstrates how both the spatially-varying sky and more than 99 per cent of the stellar sources were removed by the subtraction process. Figure 2 shows a previously known WR star in that field. Despite the lack of PSF fitting, residual artefacts for the non-emission sources are quite minimal compared to the strong residual-emission PSF of the WR star.

The final determination of candidates from the difference images involved a 3-step process. Each difference image contained many residuals that were the product of bad subtractions instead of true stellar-line emission; these must be removed. First, we determined the magnitude of every star which produced a significant positive residual in the difference image (m_{diff}), and normalised this magnitude by the original magnitude of the star in the CNB images ($m_c = (m_{c1} + m_{c2})/2$) to produce $\Delta m = m_{diff} - m_c$, a metric conceptually similar to equivalent width.

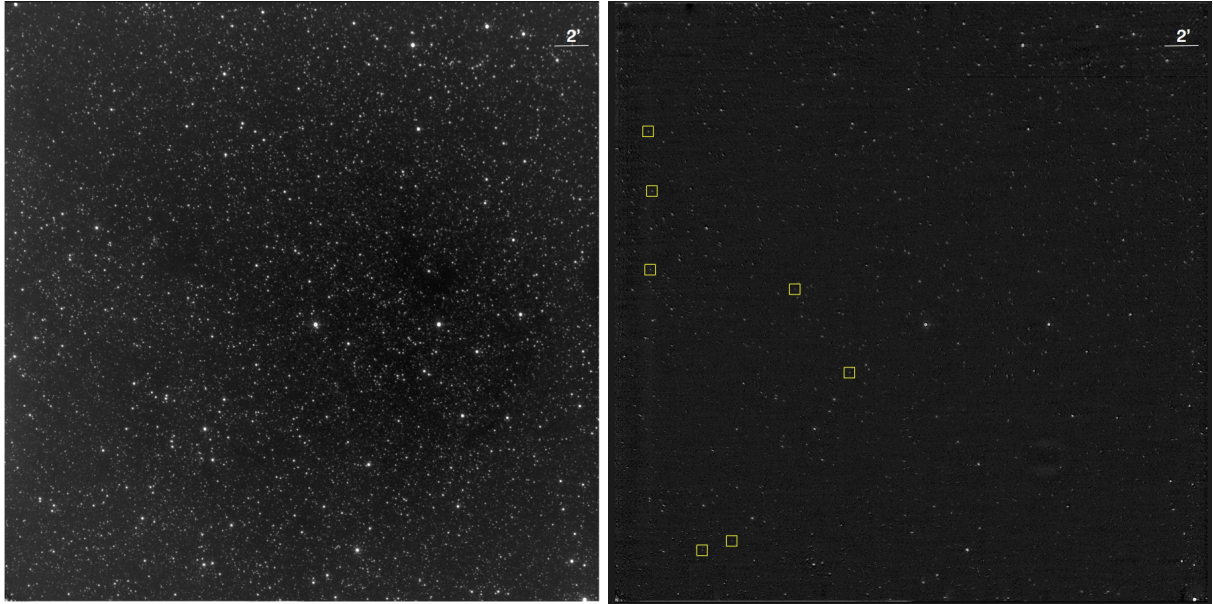
We then plotted m_c vs Δm for each filter, including a large number of fields on each plot, and determined isodensity contours. Then, m_c vs Δm was plotted for each filter in each individual field, and the 99 per cent density contour was overlaid. Only those sources with significant bright deviations outside the 99 per cent contour were considered as candidates, to eliminate field stars with no emission that survived the subtraction due to random fluctuations and poor PSF matches.

Figure 3 shows the Δm plot for the C IV filter in field 1093. Determining the optimal region of the Δm plot for strong WR characteristics was accomplished by plotting previously known Wolf–Rayet stars, and identifying areas where particular types seemed clustered, particularly with separation from the main density of residual field stars. By overplotting smoothed 99 per cent density contours on to these diagnostic plots, we were able to isolate strong candidates for further refinement.

Table 1. Predicted candidate strength in survey filters, with central wavelength and FWHM

Filter Name	He I	C IV	Br γ /He I	He II
λ (μm)	2.062	2.081	2.169	2.192
$\Delta\lambda$ (μm)	0.010	0.020	0.020	0.020
Early WN	none - very weak	none ^a	weak	strong - very strong
Late WN	very strong	none ^a	very strong	weak - strong
Early WC	weak - strong	very strong	none	none - very weak
Late WC	weak - strong	very weak - weak	very weak	none - weak
WO	none	weak	strong	weak

^a WNs may be detected in the C IV filter due to the wings of a strong He I line. This is a much more likely occurrence in WNLs than WNEs because of the relative strength of the He I line.



(a) A quadrant of the C IV image from field 1093 (a representative survey field), before image differencing. (b) The same image, after image differencing, with known Wolf-Rayet stars indicated.

Figure 1. A demonstration of the results of image differencing. We subtract a narrow-band continuum image from the narrow-band emission-line-centred image; both are scaled to the same wavelength and intensity, so that most stars should subtract to zero. This image demonstrates the high degree of crowding present in the survey images (the displayed field is $\sim 24^\circ$ from the Galactic centre). Residuals ideally are candidate emission objects. The great majority of point sources have been completely removed; residual flux from most of the remaining non-emission stars is due to incomplete subtractions of saturated stars ($K \leq 9$), or from inadequate PSF matching due to high spatial variability in the PSF between and within the images. Previously-known WR stars from the literature are identified with yellow squares in figure 1b.

The second step of the selection process was to apply MIR and NIR colour cuts. We matched every source in each image to entries in the *2MASS* and *WISE* (Wright et al. 2010) point source catalogues, and applied the following colour cuts, as per Faherty et al. (2014):

$$\begin{aligned}
 J - K_s &< 3.23(H - K_s) - 0.296 \\
 W1 - W2 &> 0.125(J - K_s) + 0.025
 \end{aligned}$$

The left panel of figure 4 is a colour-colour diagram showing the NIR colour cut, using *2MASS* colours only. The great majority of WR stars lie below the cut line, while the great majority of field stars lie above it. In the right panel, a colour-colour plot including colours from the *WISE* photometry, the separation is even more pronounced. WR

stars are intrinsically very hot, and therefore blue, and so it should come as no surprise that no WR stars lie below the cut line, with at least a 0.2 magnitude separation from the main bulk of field stars (chosen at random from the *2MASS* and *WISE* catalogues). The physical reason for the positions of WR stars on the colour-colour diagrams in figure 4 is discussed in detail in Faherty et al. (2014).

Figure 4 also includes a selection of Galactic planetary nebulae (PNe), selected from the Strasbourg-ESO catalogue (Acker et al. 1992), which are one of the primary contaminants in the emission-line candidate sample. The third and final step was to visually blink all candidates that both satisfied the colour cuts and had significant deviations on the Δm plot; this method serves to remove PN contaminants

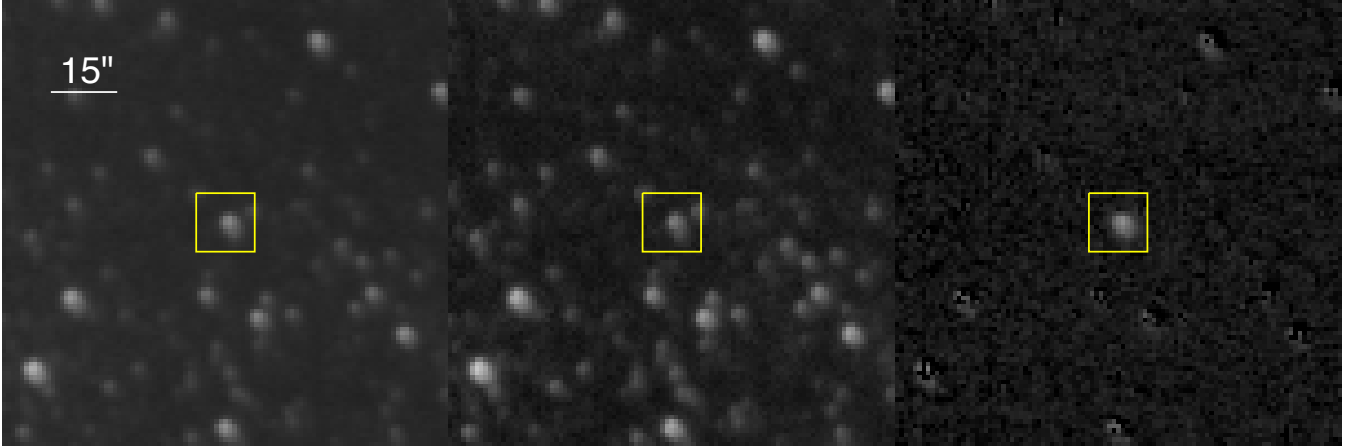


Figure 2. A zoomed portion of the image in figure 1, highlighting a known WR star in the C IV narrow band image (left), C IV interpolated continuum image (centre), and difference image (right). The WR star remains as a perfect residual PSF in the difference image, while the great majority of source pixels elsewhere are removed by the subtraction process, leaving only the brightest sources in the original C IV image as incomplete subtractions.

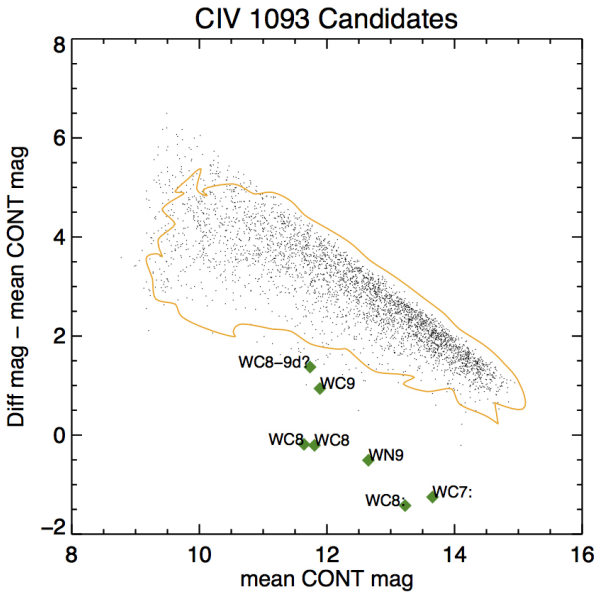


Figure 3. The diagnostic (Δm) plot for field 1093, in the C IV filter (the the image shown in figures 1 and 2). The difference image magnitude (m_{diff}) on the y-axis has been normalised for the original source brightness by subtracting continuum magnitude (m_c), leaving Δm the normalised emission-line excess. By enclosing 99 per cent of the points in the orange isodensity contour, we isolate those sources with excess that are least likely to be incomplete subtractions; known WR stars in this field, the green labelled points, lie well outside the contour. To survive the culling process, prospective candidates must lie below the contour, in a similar region to the WRs from the literature.

which are resolved, and (along with other colour cuts) removes the great majority of likely PNe from the candidate list.

3 SPECTRAL FOLLOW-UP & REDUCTION

The first round of spectral follow-up for this candidate set was conducted over 7 nights at MDM and 12 half-nights at IRTF in 2011 June and July.

3.1 IRTF

At the 3m NASA Infrared Telescope Facility (IRTF), we obtained NIR spectra of 150 candidate WR stars, selected using the criteria above, with the SpeX spectrograph. Two of the nights were cloudy enough to prevent observations. We operated in cross-dispersed mode with the 0.5" slit aligned and obtained an average resolving power of $\lambda/\Delta\lambda \sim 1200$, over a wavelength range of 0.8 – 2.4 μm .

We first acquired each target in the guider camera, then took a single AB dither pattern, with exposure times varying from 30 s for our brightest targets to 200 s for our faintest. Once we had confirmed the presence of emission lines we began a second set of AB images so each WR candidate had four images obtained with an ABBA dither pattern along the slit. To minimize the overhead (slew and calibration target time) between sources, we chose nearby subsequent targets.

After each several targets (typically 4-5), we observed an A0V star at a similar airmass for flux calibration and telluric correction. Internal flat-field and Ar arc lamp exposures were also acquired for pixel response and wavelength calibration, respectively. Additionally, we acquired spectra of almost all known spectral subtypes of Wolf-Rayet star. We reduced all data with SPEXTOOL version 3.3 (Vacca, Cushing, & Rayner 2004; Cushing, Vacca, & Rayner 2004) using standard settings.

3.2 MDM 2011

During a run of excellent weather over the 7 nights in 2011 June, we obtained 113 NIR spectra of candidate stars using TIFKAM in spectroscopic mode on the 2.4 m Hiltner telescope at MDM Observatory. The weather conditions were

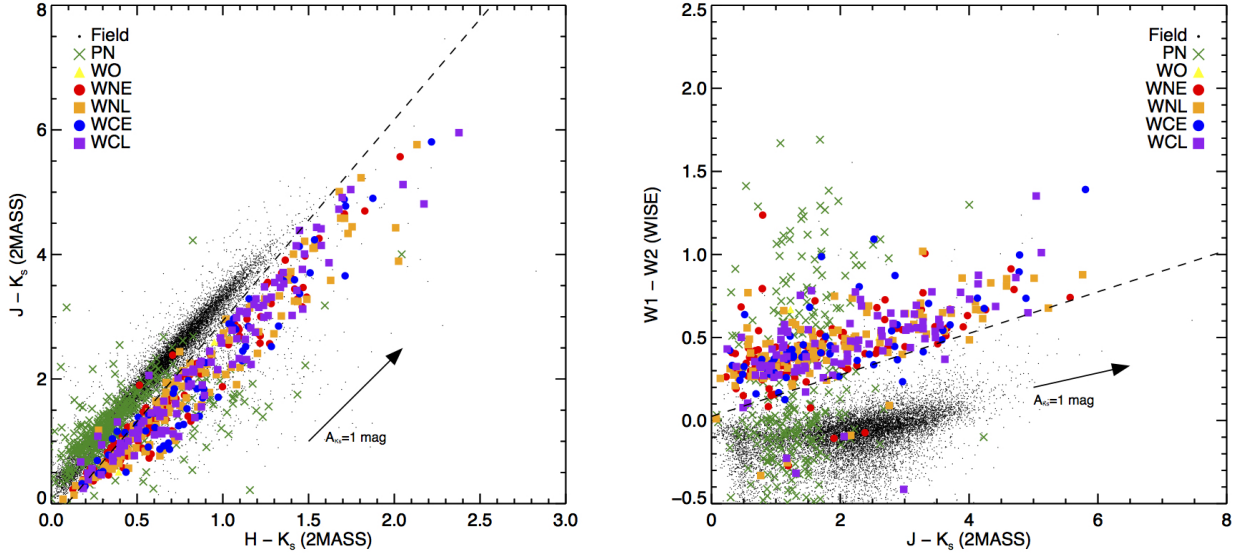


Figure 4. The second diagnostic tool for candidate selection: colour cuts from NIR (*2MASS*) and MIR (*WISE*) magnitudes. Left shows a colour-colour diagram in the NIR only, while the right includes both NIR and MIR colours. These are analogous to the figures in Mauerhan, Van Dyk, & Morris (2011), described in more detail in Faherty et al. (2014). These plots provide another layer of differentiation during the selection process. PNe are included as common emission objects other than WR stars which can be found using these tools; 18 newly-identified PNe are presented in this paper. $A_{K_s} = 1$ reddening vectors have been added, using the values for $A_{[\lambda]}/A_{K_s}$ from Indebetouw et al. (2005); the values for [3.6] and [4.5] were used for *WISE* filters W1 and W2, as the central wavelengths are sufficiently similar. The right figure in particular shows the wide separation between emission objects (WR stars and PNe) and field stars in NIR/MIR colour space.

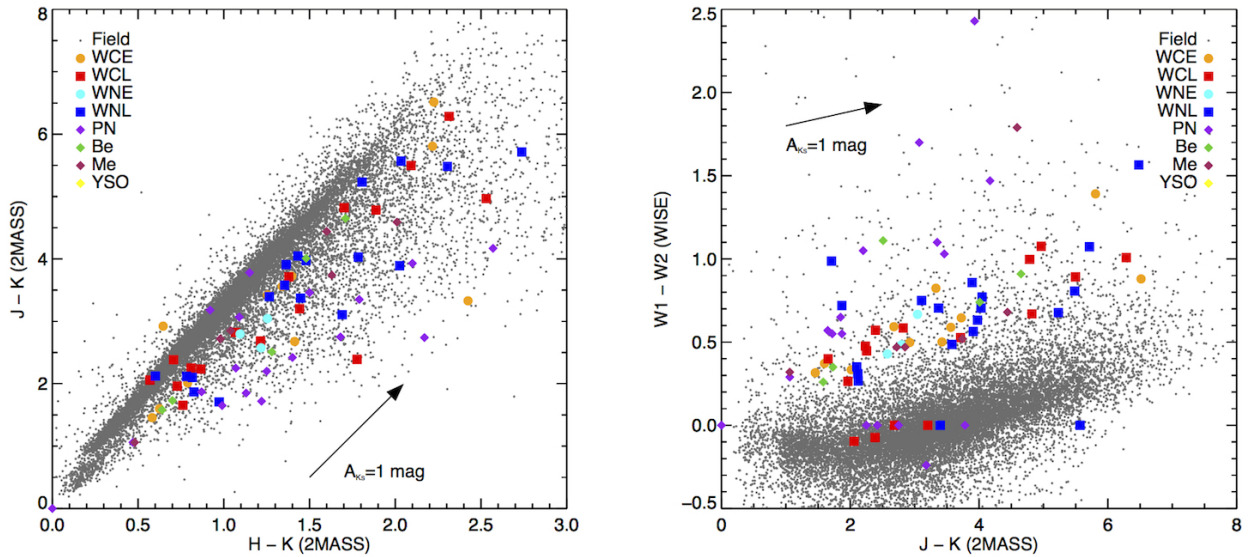


Figure 5. Colour-colour plots like those in figure 4, displaying the NIR (left) and MIR (right) colours for the new emission-line objects classified in this work. Grey dots are field stars; orange and cyan circles are early-type WCs and WNs respectively, while red and blue squares are late-type WCs and WNs. Purple diamonds are PNe, green diamonds are Be stars, brown diamonds are emitting M-giants and supergiants, and yellow diamonds are probable YSOs. Three new WR stars are below the cut line in the right panel; these have extremely close neighbours which lie on the same *WISE* pixel and confuse the magnitudes. The reddening vectors are as in figure 4.

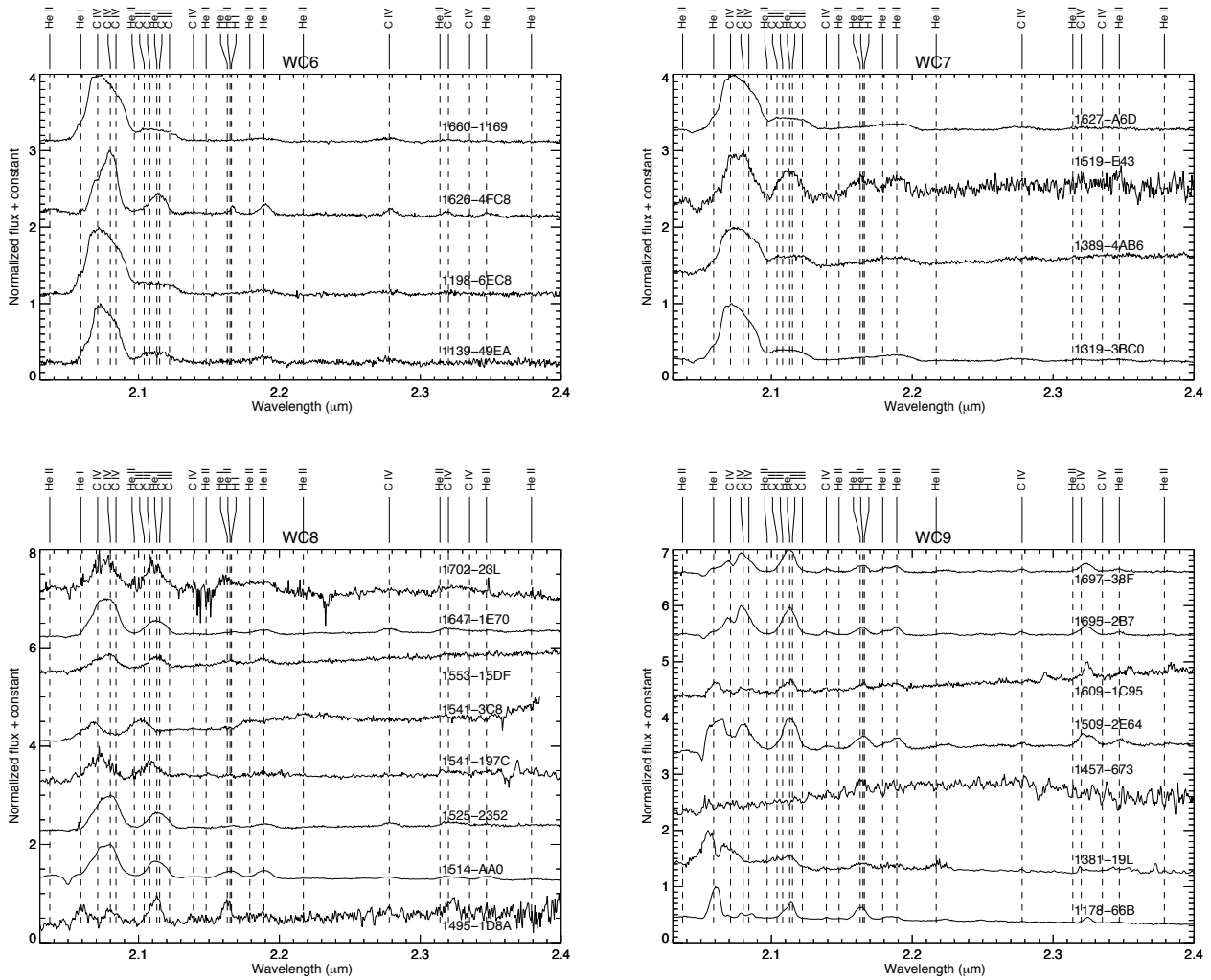


Figure 6. All new WC6 (top left), WC7 (top right), WC8 (bottom left), and WC9 (bottom right) objects classified in this work. Note the characteristic extremely strong C IV lines in the early WC6s.

excellent, with average seeing $\sim 1.5''$. We operated with the 100 μm slit, the K blocking filter, and the J/K grism, providing wavelength coverage of $1.97 - 2.42 \mu\text{m}$ at a resolving power of $\lambda/\Delta\lambda \sim 660$. We performed a single AB dither pattern on each source once it had been placed on the slit in movie mode and a guide star acquired. If on-the-fly extraction using IRAF showed emission, a second AB dither was taken, giving each WR candidate an ABBA dither pattern along the slit. Exposure times varied from 20 s for the brightest targets to 240 s for the faintest. We also observed A0V stars at a variety of airmasses for flux calibrations and telluric corrections, acquiring internal flat-field exposures as well for calibrating pixel response. Additionally, we obtained spectra of almost all known spectral subtypes of Wolf-Rayet star.

Spectra from this run were reduced with a combination of IRAF packages and IDL programs. Trimming and flat-fielding were performed with CCDPROC and FLATCOMBINE, and extraction was performed with APALL, all in IRAF. Image arithmetic, wavelength calibration, and combining extracted spectra were done in IDL; we used the XTELLCORGENERAL

program included in the SPEXTOOL package, also written in IDL.

We discovered after the run that the NeAr arc lamp images we took at the telescope were faulty, and so wavelength calibration was performed using night sky lines taken from the unprocessed images. The resulting wavelength calibration is in some cases mediocre, but there was a good enough match to perform telluric corrections, as well as to assign WR star types and subtypes.

3.3 MDM 2012

During early 2012, the original survey data were reduced again, using different methods to produce better images. A new IDL pipeline was constructed, creating flat and sky images by median-combining the first and last dither of each pointing for the entire month, using high-quality data images instead of relatively poor dome flats. Then, during a 10-day observing run in the summer of 2012 (with 6 usable nights), we obtained 70 additional NIR spectra of candidate

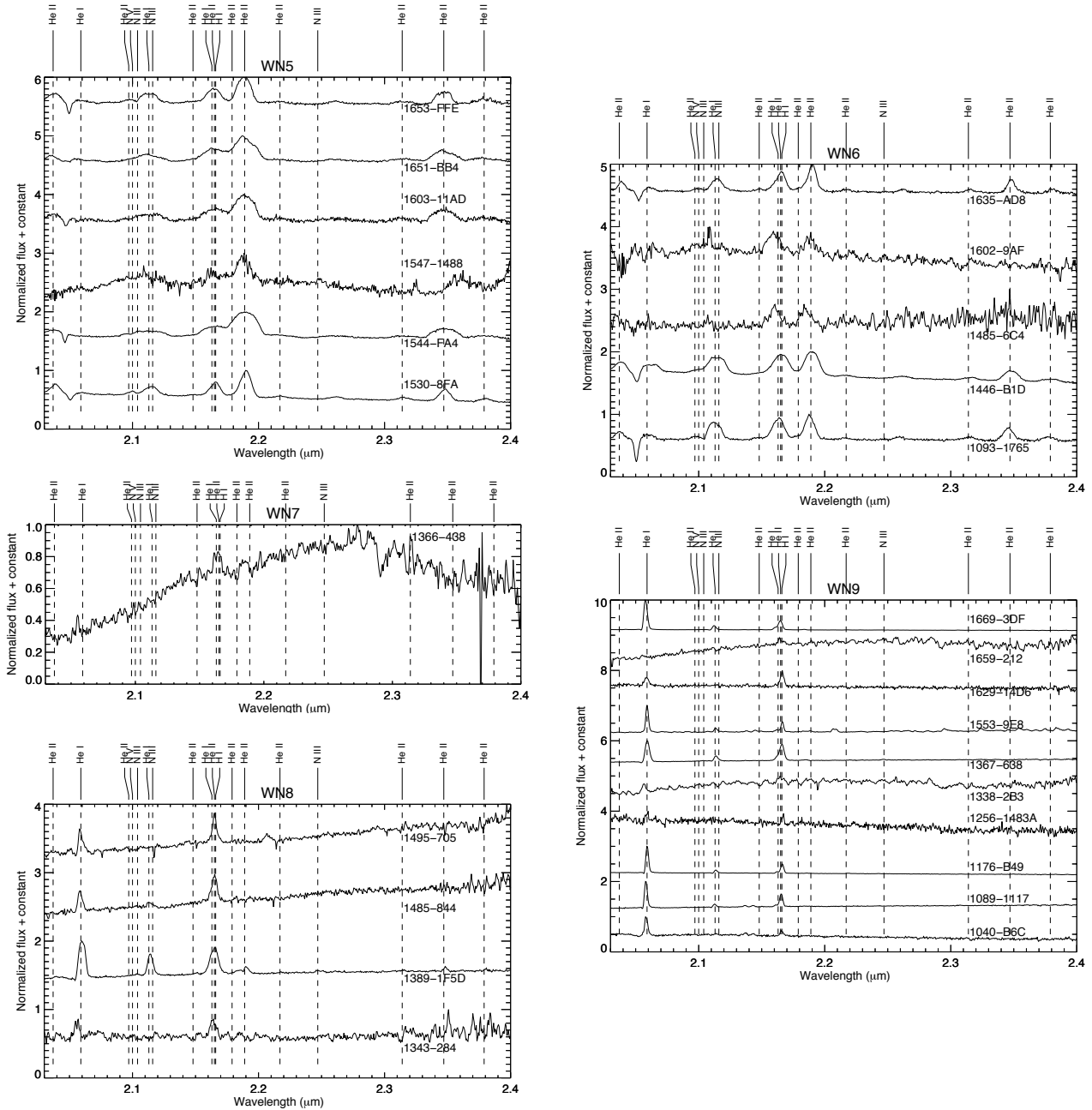


Figure 7. All new WN5 (top left), WN6 (top right), WN7 (middle left), WN8 (bottom left), and WN9 (bottom right) objects classified in this work. Object 1089-1117 (cLBV transitioning to WNL) is included, as the spectral lines are similar to those of a WN9.

stars with TIFKAM at MDM, with the same instrument setup as in 2011.

Reductions were performed entirely in IRAF, primarily using the KPNO SLIT and ONEDSPEC packages. We used a selection of long and short exposure flats to create a bad pixel mask with CCDMASK, and then performed trimming, bias-subtraction, and flat-fielding with CCDPROC and FLATCOMBINE. Once the initial preparation was complete, the spectra were extracted from the A-B images with APALL. Then we used IDENTIFY to determine a wavelength solution for each spectrum from the 4 or 5 strong Ar lines, and DISPCOR to apply the solutions to the spectra. All spectra for each in-

dividual object were combined using SCOMBINE, and then telluric correction was performed with TELLURIC.

4 RESULTS

During 29 nights of observing we observed 333 candidates, finding 89 NIR emission sources (for a success rate of 27 per cent) in some of our survey's most crowded fields. Of the emission-line sources, 49 were WR stars, 43 of which had never been previously identified, with 23 WC and 26 WN; finder charts for these new WR stars are included in

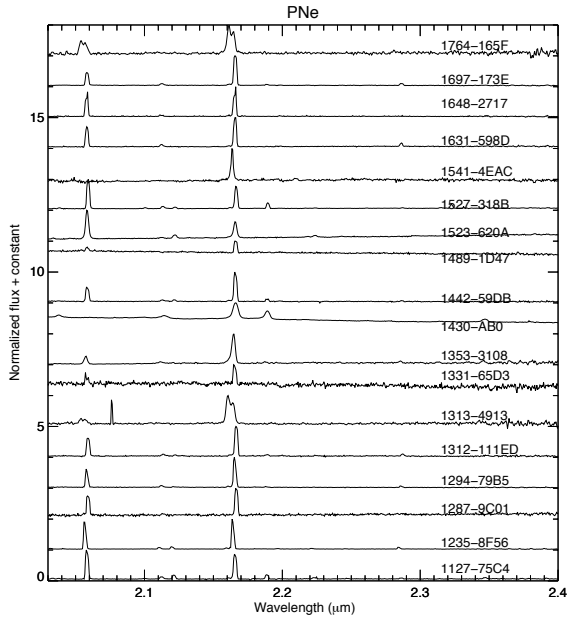


Figure 8. All new PNe classified in this work. Note the doubled emission lines for 3 of the PN spectra. The selection criteria used to identify strong Wolf-Rayet candidates are also extremely effective at identifying new PNe; the search for new PNe is described in a paper in preparation.

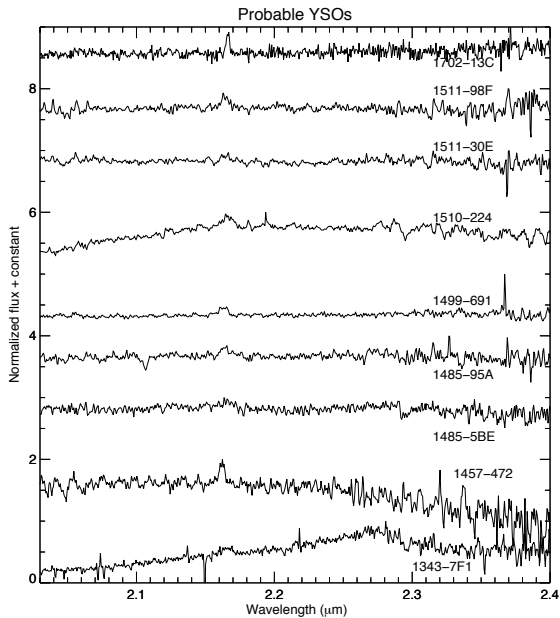


Figure 9. Likely YSOs, as these spectra lack the CO bands redwards of 2.3 μm which identify emitting red giants and supergiants.

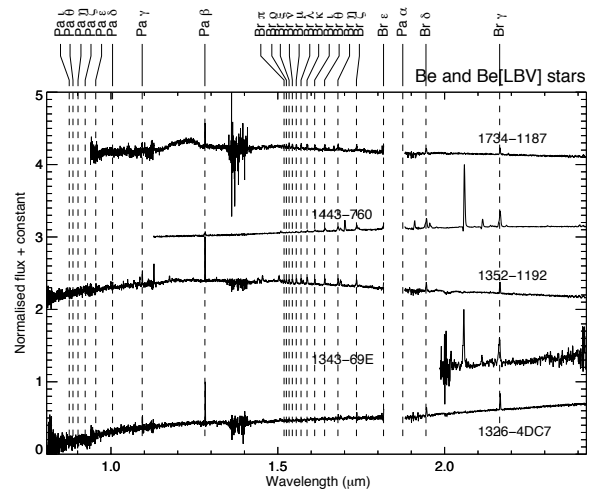


Figure 10. All new Be stars classified in this work. The full JHK spectrum is shown for these objects, displaying the prominent Hydrogen lines for those spectra for which we have J and H coverage. Be star interlopers are relatively common, as they are selected strongly by the BrGamma filter and can only be ruled out by obtaining spectra. Paschen and Brackett series emission lines are identified.

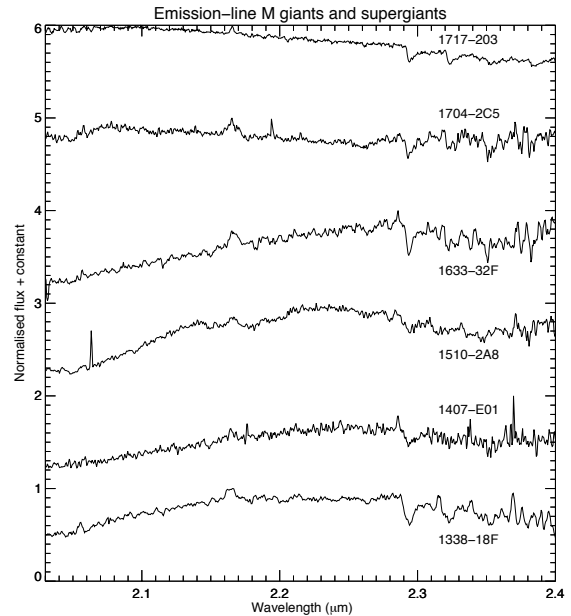


Figure 11. Red giants or supergiants, with molecular CO bands redwards of 2.3 μm , which showed H I emission.

appendix A. WR types and subtypes were assigned by eye, comparing the relative strengths of nearby line pairs as in Crowther et al. (2006); classification would ideally be performed using EWs of the spectral lines, but in many cases they are difficult to obtain due to heavy blending which is easily compensated for by eye. Figure 5 shows the positions of the new emission sources on the colour cut plots, and fig-

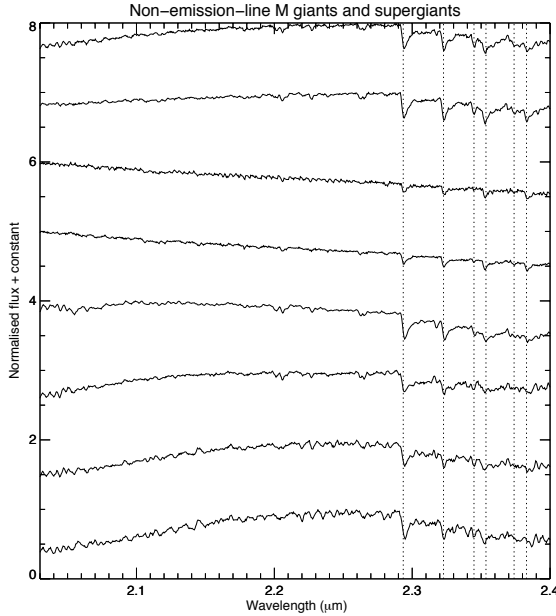


Figure 12. A selection of non-emitting red giants or supergiants. These interlopers are selected simply because the slope of the red spectrum makes them brighter in C IV than in He I or the nearest continuum filter. The dotted lines indicate the $^{12}\text{C}^{16}\text{O}$ bandheads for $v = 2 - 0$ (2.2935 μm), $v = 3 - 1$ (2.3227 μm), $v = 4 - 2$ (2.3535 μm), and $v = 5 - 3$ (2.3829 μm), and the $^{13}\text{C}^{16}\text{O}$ bandheads for $v = 2 - 0$ (2.3448 μm) and $v = 3 - 1$ (2.3739 μm).

ures 6 and 7 show the spectra of the new WR stars, sorted by subtype. Tables 2 through 6 give the location, magnitude, subtype, and (for the confirmed WR stars) extinction for each NIR emission object classified in this paper. In addition, table 7 shows the wavelengths and transitions for the WR emission lines marked in figures 6 and 7, and the measured equivalent widths are given in tables 8 thru 11.

For a number of WR stars, the *2MASS* magnitudes were not reliable (upper limits, poor photometric quality or PSF fitting, etc., as described in table 4). In such cases, the *J* and/or *CONT2* magnitudes from the survey described in section 2 were used in place of the *2MASS J* and *K_s* magnitudes, respectively. The alternate magnitudes were scaled (as were all other magnitudes from that survey, during the reduction process) to match those given in *2MASS*. However, if the *2MASS H* magnitude could not be used, or the alternate *J* or *CONT2* magnitudes were unavailable, then extinction and distance were not calculated.

One of the confirmed WR stars is particularly notable: 1627-A6D, a WC7:: which is associated with a *Chandra* x-ray source (CXO J191011.5+085839); no other WRs described here were successfully matched to *Chandra* sources. 1627-A6D was originally identified in Smith et al. (2012), also as a WC7. Using the relation $A_K/A_V = 0.112$ from Rieke & Lebofsky (1985) with the calculated A_{K_s} of 3.0 (table 6), we derive a *V*-band extinction of 26.8 for $R = 3.11$ extinction. Then, we derive the hydrogen column density as in Predehl & Schmitt (1995), arriving at $N_h = 4.82 \times$

10^{22} cm^{-2} . This source has an ACIS-broad x-ray flux of $3.1 \times 10^{-14} \text{ erg s}^{-1} \text{ cm}^{-2}$, and assuming a characteristic temperature of 1 keV, an unabsorbed flux of $4.1 \times 10^{-13} \text{ erg s}^{-1} \text{ cm}^{-2}$ (calculated via WebPIMMS¹). Using the calculated distance shown in table 6, we find an x-ray luminosity of $1.7 \times 10^{33} \text{ erg s}^{-1}$, which is consistent with other WN x-ray luminosities, but two orders of magnitude higher than the WCs in Skinner et al. (2006). For a characteristic temperature of 3 keV, this becomes an unabsorbed flux of $1.0 \times 10^{-13} \text{ erg s}^{-1} \text{ cm}^{-2}$ and an x-ray luminosity of $3.4 \times 10^{32} \text{ erg s}^{-1}$; if the characteristic temperature is 10 keV, the unabsorbed flux would be $7.6 \times 10^{-14} \text{ erg s}^{-1} \text{ cm}^{-2}$, for an x-ray luminosity of $2.5 \times 10^{32} \text{ erg s}^{-1}$. As there are no known single WC stars which show x-ray emission, it is statistically most likely that 1627-A6D is a colliding-wind binary, but without more extensive x-ray spectroscopy, we cannot discount the possibility of a WC7 + compact companion.

In addition to new WR stars, we classified a number of other emission-line objects which were selected using our tools. The 17 planetary nebulae (spectra shown in figure 8) display strong emission in the He I 2.06 μm and Br γ /He I 2.17 μm filters, with little to no continuum. PNe are quite easy to identify, particularly using *2MASS* and *WISE* colour criteria, as described in Faherty et al. (2014) and a paper in preparation. We also observed nine emission-line sources which are likely to be emitting YSOs (cf. Greene & Lada 1996) due to the lack of CO bands redwards of 2.3 μm ; these spectra are shown in figure 9.

Another source of interlopers in the WR candidate set is Be stars (see also Faherty et al. 2014; Mauerhan et al. 2010); the 5 Be spectra are shown in figure 10. These spectra show relatively weak emission in the 2.17 μm filter, with strong continuum emission and a large number of hydrogen lines, especially in the H-band. Finally, the largest category of contaminants amongst our candidates are M giants and supergiants, often with Br- γ emission, as shown in figures 11 and 12 (cf. Rayner, Cushing, & Vacca 2009). Contaminants with no emission were generally chosen using criteria from the He II and Br- γ filters early on in the selection process; due to the shape of the spectra, these stars appeared brighter in those filters than in at least one of the continuum filters. Once we discovered this trend, that criterion was no longer used.

5 GALACTIC WR DISTRIBUTION

We expect to find WR stars in areas with recent star formation, which in spiral galaxies like the Milky Way will be in the plane of the Galaxy, concentrated most closely along the spiral arms. Figure 13 shows a plot of the distribution of confirmed WR stars as projected on to the sky, using absolute-magnitude calibrations for the various WR types from Rosslowe & Crowther (2015), and coordinates from the Galactic Wolf-Rayet Catalogue associated with the same publication². As expected, the WR stars cluster strongly within 1° of $b = 0$; 80 per cent of all confirmed WR stars

¹ <https://heasarc.gsfc.nasa.gov/cgi-bin/Tools/w3pimms/w3pimms.pl>

² <http://pacrowther.staff.shef.ac.uk/WRcat/index.php>

Table 2. Spectroscopically-confirmed Wolf-Rayet stars. Objects are identified by field number and object number; this has no relation to RA or Dec. In addition, it is difficult to differentiate between features of WC4 – 8. A colon (:) indicates an uncertainty of up to ± 2 subtypes.

Name	δ (J2000)	δ (J2000)	l	b	Type	Telescope
1040-B6C	16 04 03.76	-53 10 44.2	-30.54	-0.527	WN9	IRTF
1089-1117	16 31 37.79	-48 14 55.3	-23.98	-0.038	cLBV/WNL ¹	IRTF
1093-1765	16 32 25.70	-47 50 46.1	-23.60	0.139	WN6	IRTF
1139-49EA	16 54 08.46	-43 49 25.3	-18.09	-0.073	WC6::	IRTF
1178-66B	17 07 23.95	-39 19 54.4	-13.02	0.738	WC9	IRTF
1176-B49	17 12 34.87	-40 37 13.8	-13.47	-0.827	WN9h	IRTF
1198-6EC8	17 15 55.90	-37 19 12.0	-10.41	0.575	WC6::	IRTF
1256-1483A	17 40 59.36	-32 11 22.1	-3.292	-0.860	WN9	IRTF
1319-3BC0	17 57 16.87	-25 23 13.8	4.376	-0.416	WC7:	IRTF
1338-2B3	17 59 07.99	-22 36 43.0	6.991	0.605	WN9	MDM12
1343-284	18 03 28.37	-22 22 58.9	7.686	-0.152	WN8-9	MDM12
1366-438	18 05 55.27	-19 29 44.1	10.483	0.765	WN7-8 ²	MDM12
1367-638	18 09 06.22	-19 54 27.2	10.487	-0.090	WN9	IRTF
1381-19L	18 12 02.41	-18 06 55.4	12.392	0.167	WC9	MDM11
1389-4AB6	18 14 14.09	-17 21 02.6	13.313	0.075	WC7	IRTF
1389-1F5D	18 14 17.37	-17 21 54.4	13.307	0.057	WN8	IRTF
1446-B1D	18 25 00.25	-10 33 23.5	20.536	0.983	WN6 ³	IRTF
1457-673	18 31 06.65	-09 48 01.4	21.904	0.004	WC9d	MDM12
1485-6C4	18 36 55.53	-06 31 02.1	25.480	0.241	WN6	MDM12
1485-844	18 37 51.82	-06 31 19.1	25.583	0.032	WN8	MDM12
1495-1D8A	18 39 40.60	-05 35 17.6	26.620	0.059	WC8-9	MDM12
1495-705	18 39 41.19	-05 57 36.3	26.290	-0.113	WN8	MDM12
1514-AA0	18 41 06.79	-02 56 01.0	29.144	0.957	WC8	IRTF
1509-2E64	18 42 26.61	-03 56 36.0	28.398	0.199	WC9	IRTF
1525-2352	18 45 14.63	-02 05 05.7	30.370	0.427	WC8:	IRTF
1519-E43	18 45 49.88	-02 59 56.0	29.624	-0.121	WC7 ⁴	MDM12
1530-8FA	18 46 00.97	-01 14 35.0	31.207	0.639	WN5	IRTF
1541-3C8	18 50 02.75	-00 32 07.9	32.297	0.066	WC8 ⁴	MDM11
1541-197C	18 50 37.54	-00 01 21.1	32.819	0.171	WC8	MDM11
1544-FA4	18 51 33.09	-00 13 40.8	32.742	-0.129	WN5	IRTF
1553-9E8	18 52 33.12	+00 47 41.8	33.766	0.115	WN9h	IRTF
1547-1488	18 52 57.20	+00 02 54.1	33.148	-0.315	WN5	MDM11
1553-15DF	18 53 02.56	+01 10 22.7	34.159	0.178	WC8	IRTF
1602-9AF	19 02 42.32	+06 54 44.4	40.365	0.657	WN6	MDM11
1603-11AD	19 04 20.14	+06 07 52.2	39.856	-0.061	WN5	IRTF
1609-1C95	19 06 10.68	+07 19 13.3	41.123	0.078	WC9	IRTF
1626-4FC8	19 06 33.66	+09 07 20.8	42.767	0.822	[WC6:] ⁵	IRTF
1629-14D6	19 10 06.40	+09 45 25.7	43.733	0.339	WN9h	IRTF
1627-A6D	19 10 11.53	+08 58 39.6	43.051	-0.040	WC7:: ⁴	IRTF
1635-AD8	19 13 19.19	+09 55 29.0	44.248	-0.285	WN6	IRTF
1653-FFE	19 14 40.73	+11 54 15.4	46.156	0.338	WN5-6	IRTF
1651-BB4	19 15 37.26	+11 25 26.3	45.838	-0.089	WN5	IRTF
1647-1E70	19 15 52.52	+11 12 59.7	45.683	-0.241	WC8:	IRTF
1659-212	19 17 22.20	+12 13 09.2	46.741	-0.097	WN9	MDM12
1669-3DF	19 18 31.35	+13 43 39.4	48.206	0.360	WN9h	IRTF
1660-1169	19 20 02.46	+12 08 20.3	46.975	-0.712	WC6:	IRTF
1697-38F	19 25 18.12	+17 02 15.9	51.895	0.477	WC9	IRTF
1702-23L	19 26 08.35	+17 46 23.1	52.637	0.651	WC8	MDM11
1695-2B7	19 27 17.98	+16 05 24.6	51.289	-0.394	WC9	IRTF

¹ Originally identified in Gvaramadze, Kniazev, & Fabrika (2010) (MN42), and then re-classified as a cLBV transitioning to late WN in Stringfellow et al. (2012).² Possibly an emitting M-giant.³ Originally identified in Hadfield et al. (2007) (HDM 10).⁴ Originally identified in Smith et al. (2012) (2w06, 2w10, 2w11).⁵ Originally classified as a [WC] in Gvaramadze, Kniazev, & Fabrika (2010) (MN102); the brackets indicate a central star of a Planetary Nebula, which displays WR-like emission.

Table 3. Other NIR emission sources. Objects are identified by field number and object number; this has no relation to RA or Dec.

Name	δ (J2000)	δ (J2000)	l	b	Type ^a	Telescope
1127-75C4	17 29 37.54	-35 13 43.8	-7.126	-0.515	True PN ¹	IRTF
1235-8F56	17 31 50.69	-34 10 44.3	-5.999	-0.319	PN	IRTF
1294-79B5	17 46 01.68	-27 26 01.3	1.33	0.706	Possible PN ²	IRTF
1287-9C01	17 47 14.65	-28 26 48.8	0.603	-0.05	PN	IRTF
1313-4913	17 52 59.34	-25 27 28.1	3.825	0.385	Likely PN ²	MDM12
1326-4DC7	17 56 28.55	-24 00 27.1	5.477	0.435	Be	IRTF
1312-111ED	17 56 41.57	-26 31 09.5	3.33	-0.869	PN	IRTF
1338-18F	17 58 57.24	-22 20 24.6	7.206	0.776	^a	MDM12
1331-65D3	17 59 42.43	-23 51 43.7	5.972	-0.132	PN	IRTF
1343-69E	18 02 22.35	-22 38 00.3	7.343	-0.055	B[e]/LBV ^b	MDM12
1343-7F1	18 02 44.42	-22 19 36.7	7.651	0.023	^c	MDM12
1353-3108	18 04 08.45	-20 57 05.8	9.009	0.416	Likely PN ³	MDM12
1352-1192	18 06 40.77	-21 40 17.4	8.67	-0.452	Be	IRTF
1407-E01	18 18 58.19	-15 49 37.9	15.193	-0.198	^a	MDM12
1430-AB0	18 21 02.92	-12 27 45.8	18.397	0.945	PN ^d	IRTF
1442-59DB	18 24 07.91	-11 06 42.6	19.945	0.913	True PN ²	IRTF
1443-760	18 28 33.39	-11 46 44.2	19.860	-0.358	B[e]/LBV ^b	IRTF
1457-472	18 29 40.38	-09 31 21.5	21.986	0.447	^c	MDM12
1485-5BE	18 36 16.87	-06 43 17.6	25.225	0.289	^c	MDM12
1485-95A	18 37 14.85	-06 44 44.4	25.314	0.065	^c	MDM12
1489-1D47	18 37 30.41	-06 14 15.0	25.795	0.241	PN	IRTF
1510-224	18 39 43.87	-03 34 43.5	28.412	0.968	^c	MDM12
1499-691	18 40 36.84	-05 27 24.5	26.843	-0.088	^c	MDM12
1510-2A8	18 41 33.60	-03 39 05.9	28.556	0.529	^a	MDM12
1511-30E	18 44 05.00	-03 57 02.4	28.578	-0.168	^c	MDM12
1511-98F	18 44 18.19	-04 05 07.1	28.483	-0.278	^c	MDM12
1523-620A	18 47 00.40	-02 27 51.6	30.234	-0.138	Possible PN ⁴	IRTF
1527-318B	18 48 29.26	-02 10 01.4	30.667	-0.332	Possible PN ⁴	IRTF
1541-4EAC	18 49 45.18	-00 29 08.0	32.308	0.154	PN	MDM11
1633-32F	19 10 37.97	+09 47 34.5	43.824	0.240	^a	MDM12
1631-598D	19 10 56.59	+09 28 36.6	43.579	0.026	PN	IRTF
1648-2717	19 16 30.50	+10 40 56.3	45.283	-0.628	PN	IRTF
1702-13C	19 25 15.87	+17 31 40.7	52.323	0.718	^c	IRTF
1697-173E	19 25 53.53	+16 53 31.5	51.834	0.284	Likely PN ⁴	IRTF
1717-203	19 30 57.41	+19 29 51.8	54.698	0.473	^a	IRTF
1704-2C5	19 32 03.38	+16 44 42.4	52.411	-1.082	^a	MDM12
1734-1187	19 32 28.69	+21 11 30.4	56.354	0.976	Be	IRTF
1764-165F	19 45 32.87	+23 28 10.4	59.823	-0.536	Likely PN ⁴	MDM12

^a These stars are emitting cool stars, M giants or supergiants (Rayner, Cushing, & Vacca 2009).

^b Originally identified in Wachter et al. (2011).

^c A number of emission sources seem likely to be YSOs (Greene & Lada 1996).

^d This object is missing the P Cygni absorption lines normally seen in a WN7h, and so is likely a high-ionisation nebula.

¹ Originally identified in Miszalski et al. (2008).

² Originally identified in Acker et al. (1992).

³ Originally identified in Kerber et al. (2003).

⁴ Originally identified in Urquhart et al. (2009).

lie within the bounds of the survey described in section 2, despite being limited to $\pm 1^\circ$ in Galactic latitude. Also included in figure 13 is a histogram showing the distribution of WR stars in Galactic longitude. The plot shows heavy clustering at $l = \pm 30^\circ$, where the telescope is pointed along the Carina or Norma arms, as predicted in simulations of WR distribution based on local surface densities, described in the appendix to Paper I.

Figure 16 shows the distribution of WR stars on the Galactic plane, overlaid on an artist's representation of the Milky Way so as to highlight the spiral arms. This work (in combination with Papers I and II) more than doubles

the number of confirmed WR stars on the far side of the Galaxy, including the most distant WR stars yet identified. The majority of new WR stars classified here roughly trace the northern curve of the Carina arm, where one would expect the most massive star formation.

5.1 Completeness and the Survey in Context

The image subtraction methods detailed in section 2, in addition to the candidate selection methods described in Papers I and II, have allowed us to identify the faintest, furthest WR stars in the Galaxy. Figure 14 shows histograms

Table 4. Photometry for confirmed WR stars. *B*, *V*, and *R* photometry is from the NOMAD catalogue; *J*, *H*, and *K_s* photometry is from *2MASS*; and *W1* – 4 are from the *WISE* All-Sky Source Catalog. Upper limits are marked with >, poor photometry quality (C or worse on the PH-QUAL flag) with a colon (:), possible contamination by an asterisk (*), and poor PSF fitting with †.

Name	<i>B</i>	<i>V</i>	<i>R</i>	<i>J</i>	<i>H</i>	<i>K_s</i>	<i>W1</i>	<i>W2</i>	<i>W3</i>	<i>W4</i>	<i>J</i> – <i>K_s</i>	<i>H</i> – <i>K_s</i>	<i>W1</i> – <i>W2</i>
1040-B6C	–	–	–	13.13	11.90	11.17	10.41	10.15	> 10.74	> 8.35	1.96	0.73	0.26
1089-1117	–	–	–	> 16.57	12.60	10.28	8.53	7.53	6.58	1.62†	6.29	2.31	1.01
1093-1765	–	–	–	15.15	12.93	11.57	10.46	9.98	8.71	> 8.55	3.58	1.35	0.49
1139-49EA	–	–	–	> 16.29	> 14.53	13.09	–	–	–	–	3.20	1.44	–
1178-66B	–	–	–	12.49	11.12	10.26	9.51	9.03	8.40	6.99	2.24	0.87	0.48
1176-B49	–	–	–	12.66	11.22	10.41	9.69	9.24	8.81	> 7.86	2.25	0.81	0.45
1198-6EC8	–	–	–	> 16.15	> 14.68	13.47	–	–	–	–	2.69	1.21	–
1256-1483A	–	–	–	13.98	12.46	11.86	11.07	10.81	4.89	0.84	2.12	0.60	0.27
1319-3BC0	–	–	–	14.89:	> 12.72	> 11.46	10.89	10.39	> 8.97	> 7.58	3.42	1.26	0.50
1338-2B3	–	–	–	12.61	> 10.48	> 9.21	–	–	–	–	3.40	1.27	–
1343-284	17.39	15.60	14.72	10.47	9.60	9.02	8.40	8.08	7.68	> 5.82	1.46	0.58	0.32
1366-438	–	–	–	12.91	> 10.58	> 9.20	7.78	7.26	5.98	4.65	3.71	1.38	0.53
1367-638	–	–	–	15.96:	12.43	10.40	–	–	–	–	5.57	2.03	–
1381-19L	15.48	13.86	13.78	9.66	8.26	7.80*	7.34:	6.62	5.90	4.89	1.87	0.83	0.72
1389-4AB6	–	–	20.74	16.13	14.26	12.24	10.22	9.36	8.37	6.88	3.89	2.03	0.86
1389-1F5D	–	–	–	> 17.57	13.28	11.05	9.67	8.79	8.91	> 5.78	6.52	2.23	0.88
1446-B1D	–	–	17.24	12.21	11.24	10.61	9.68	9.31	8.30	6.95	1.60	0.63	0.37
1457-673	–	–	–	14.85	> 11.44	> 9.35	7.55	6.66	5.28	3.62	5.50	2.09	0.89
1485-6C4	–	–	16.66	12.04	10.81	10.02	9.23	8.90	8.06	> 5.30	2.02	0.79	0.33
1485-844	–	–	–	14.72	11.30	9.49	8.07	7.40	6.84	5.30	5.23	1.81	0.68
1495-1D8A	–	–	–	> 14.64	> 12.36	11.72	9.72†	9.22†	> 9.87	> 6.75	2.92	0.65	0.50
1495-705	–	–	–	14.97	11.38	9.16	7.31	5.92	4.75	3.77	5.81	2.22	1.39
1514-AA0	–	–	–	12.92	11.24	10.54	10.06	10.13	10.15	> 7.27	2.38	0.71	-0.07
1509-2E64	–	–	–	> 15.78	14.87:	12.45	9.83†	9.01†	8.33	6.36:	3.33	2.42	0.82
1525-2352	–	–	–	> 17.93	14.75	12.44	10.34†	9.53	> 9.01	> 6.23	5.48	2.30	0.81
1519-E43	–	–	–	> 13.65	13.04	11.26	9.59†	9.01	9.66:	> 7.09	2.39	1.78	0.57
1530-8FA	–	–	–	12.76	11.43	10.64	9.03	8.72	9.90	> 7.82	2.12	0.78	0.31
1541-3C8	–	–	–	> 16.98	13.86	12.15	10.73	10.06	> 8.54	> 6.28	4.82	1.70	0.67
1541-197C	–	–	–	> 14.74	13.33	> 11.64	10.05	9.30	8.73	4.45†	3.11	1.69	0.75
1544-FA4	–	–	–	> 13.50	12.24†	10.83†	9.61	9.02	8.37	> 7.17	2.68	1.41	0.59
1553-9E8	–	–	–	15.76	12.86	10.98	9.54	8.54	8.47	> 6.35	4.78	1.89	1.00
1547-1488	–	–	–	13.96	12.25	11.16	9.99	9.51	8.62	7.39:	2.80	1.10	0.48
1553-15DF	–	–	–	> 17.78	14.80	12.07	9.70	8.62	> 8.28	4.03	5.71	2.74	1.07
1602-9AF	–	–	–	13.11	11.62	11.05	10.59	10.67	9.60	7.27	2.06	0.57	-0.10
1603-11AD	–	–	–	16.13	13.64	12.16	10.43†	9.80	8.76	6.93	3.98	1.48	0.63
1609-1C95	–	–	–	> 18.41	15.07	11.93	9.91	8.35	8.58	> 8.19	6.48	3.14	1.57
1626-4FC8	–	–	17.40	15.59	14.86	13.89	12.77	11.79	5.71†	2.09†	1.71	0.97	0.99
1629-14D6	–	–	–	14.73	13.44	12.63	11.75†	11.40	> 10.42	> 7.93	2.10	0.82	0.35
1627-A6D	–	–	–	> 15.78	13.54	11.75	10.51	9.80	> 10.92	> 6.77	4.03	1.78	0.70
1635-AD8	–	–	–	15.20	12.87	11.48	10.27	9.63	9.26	8.52	3.72	1.40	0.65
1653-FFE	–	–	–	> 15.22	> 13.00	11.66	10.37	9.78	9.17	8.61:	3.56	1.34	0.59
1651-BB4	–	–	–	15.83	> 13.21	> 11.78	10.30	9.53	8.60	5.18	4.05	1.43	0.77
1647-1E70	–	–	–	> 17.53	15.10	12.57	10.74†	9.66	8.65	4.93	4.97	2.53	1.08
1659-212	–	–	–	13.44	10.89	9.53	8.56	8.00	7.06	6.00	3.91	1.36	0.56
1669-3DF	–	–	–	12.79	11.03	9.97	8.81	8.22	7.61	6.57	2.82	1.07	0.59
1660-1169	–	–	–	14.65	13.29	12.08	11.65	11.22	> 11.15	> 8.72	2.58	1.22	0.43
1697-38F	–	–	–	12.97†	11.18†	9.92	8.54	7.87	7.58	6.57	3.04	1.25	0.67
1702-23L	20.44	17.29	16.15	11.86	10.97	10.21	9.66	9.26	8.60	7.62	1.66	0.76	0.40
1695-2B7	–	–	–	13.01	11.09	9.64	8.40	7.70	7.27	7.02	3.37	1.45	0.71

and cumulative fractions of the *J* – and *K_s* – magnitudes, respectively, for WR stars identified by the Shara et al. survey and in the literature. There is a clear divergence in the range of typical magnitudes between the two populations; the WR stars identified by this survey are significantly fainter than those in the literature, particularly for WC stars, which can be far more difficult to identify if the emission lines are diluted by continuous NIR emission by the star’s shroud of

dust (a characteristic of WC9ds, particularly near the Galactic centre). In addition, figure 17 shows that these faint WR stars lie at greater distances from the Solar System than any WR stars previously identified. The Shara et al. survey has more than doubled the number of confirmed WR stars on the far side of the Milky Way.

As an independent check of our distance calculations, we plotted *K_s* – band absorption vs *2MASS K_s* magnitude

A Near-Infrared Survey of the Inner Galactic Plane for Wolf-Rayet Stars III. New Methods: Faintest WR Stars

Table 5. Photometry for other NIR emission sources. B , V , and R photometry is from the NOMAD catalogue; J , H , and K_s photometry is from *2MASS*; and $W1 - 4$ are from the *WISE* All-Sky Source Catalog. Upper limits are marked with $>$, poor photometry quality (C or worse on the PH_QUAL flag) with a colon (:), possible contamination by an asterisk (*), and poor PSF fitting with †.

Name	B	V	R	J	H	K_s	$W1$	$W2$	$W3$	$W4$	$J - K_s$	$H - K_s$	$W1 - W2$
1127-75C4	–	–	16.08	14.99	13.92	12.24	–	–	–	–	2.75	1.68	–
1235-8F56	–	–	–	> 16.48	> 13.85	12.7	–	–	–	–	3.78	1.15	–
1294-79B5	–	–	–	> 13.44	12.44	11.57	10.18†	9.63	4.33	0.54	1.87	0.87	0.55
1287-9C01	18.42	17.24	16.97	> 14.81	> 14.00	12.60	8.36†	5.02†	> 0.81	> 1.68	2.74	2.17	3.34
1313-4913	–	–	16.01	13.45	12.79	11.8	9.9†	9.33†	4.08	-0.36	1.65	0.99	0.57
1326-4DC7	–	–	–	13.91	12.68	11.4	9.12	8.01	5.46	4.11	2.51	1.28	1.11
1312-111ED	–	–	–	–	–	–	–	–	–	–	–	–	–
1338-18F	–	–	–	14.32	11.48	9.88	8.37	7.69	7.19	6.55	4.44	1.60	0.68
1331-65D3	–	–	–	15.69	> 13.43	> 12.51	11.82	12.06	6.06	1.89	3.18	0.92	-0.24
1343-69E	–	–	–	13.60	11.07	9.59	8.46†	7.72	6.67	3.64	4.01	1.48	0.73
1343-7F1	–	–	–	> 13.99	11.57†	9.47	8.21	7.38	6.5	4.72	4.52	2.10	0.83
1353-3108	–	–	–	13.82	12.8	11.40	–	–	–	–	2.42	1.40	–
1352-1192	–	–	18.13	12.99	12.05	11.41	10.56	10.30	10.29:	> 7.40	1.58	0.64	0.26
1407-E01	19.16	–	16.19	> 13.72	11.61	9.98	8.7	8.18	7.55	> 7.47	3.74	1.63	0.52
1430-AB0	17.07	15.21	16.90	11.70†	11.11†	10.64	9.92	9.63	9.12	8.19	1.06	0.48	0.30
1442-59DB	–	–	–	14.35	13.85	12.63	10.17†	9.62†	4.79	1.69	1.72	1.22	0.55
1443-760	18.40	–	14.38	14.35	11.41	9.7	8.33†	7.42†	6.72	2.93†	4.65	1.71	0.91
1457-472	–	–	–	10.59	10.19	9.84	9.14†	8.82†	7.7	5.85	0.75	0.35	0.32
1485-5BE	13.47	13.10	12.75	11.01	10.26	9.92	9.39	8.36	6.5†	2.97†	1.09	0.34	1.03
1485-95A	14.98	13.88	12.70	> 11.76	> 10.80	10.34	9.77	9.59	> 9.42	> 6.31	1.42	0.46	0.18
1489-1D47	17.34	16.14	14.80	14.08	12.12	10.62†	7.55†	6.52†	1.21	-2.04†	3.46	1.50	1.03
1510-224	–	–	–	10.1	8.43	7.56	6.95	6.53	4.93	3.72	2.54	0.87	0.42
1499-691	–	–	–	10.86	9.94	9.29	8.67	8.41	8.57	> 6.96	1.57	0.65	0.26
1510-2A8	18.79	17.69	15.52	11.1	9.29	8.25	7.32	6.85	6.59	6.37	2.85	1.04	0.47
1511-30E	–	–	18.08	9.98	9.63	9.55	9.33	9.31	8.84:	> 5.54	0.43	0.08	0.02
1511-98F	12.16	11.73	11.44	11.13	10.84	10.66	10.38	10.38	> 9.05	> 6.70	0.47	0.18	0.00
1523-620A	13.62	13.41	12.27	> 16.29	> 14.31	13.22:	> 9.54	7.84	3.08	0.03	3.07	1.09	1.70
1527-318B	–	–	–	> 16.82	14.99:	12.89	9.73	7.3	2.15	-1.2	3.93	2.10	2.43
1541-4EAC	–	–	–	15.05	13.87	12.8	–	–	–	–	2.25	1.07	–
1633-32F	–	–	18.52	14.91	12.33	10.32	5.9	4.11	1.51	0.41	4.59	2.01	1.79
1631-598D	–	–	–	> 18.25	> 16.65	14.08	12.22	10.75	5.39	2.44	4.17	2.57	1.47
1648-2717	–	–	–	> 16.44	14.88	13.09	11.55	10.45	4.83	0.99	3.35	1.79	1.10
1702-13C	–	–	–	11.5	9.72	8.99	8.54	8.62	8.68	> 7.63	2.51	0.73	-0.08
1697-173E	–	17.72	18.69	14.18	13.23	11.98	10.73	9.68	4.09	0.33	2.20	1.25	1.05
1717-203	–	–	17.4	11.95	10.21	9.23	8.04	7.57	6.83	6.01	2.72	0.98	0.47
1704-2C5	–	–	–	10.95	10.37	9.89	9.13	8.81	7.78	4.72	1.06	0.48	0.32
1734-1187	16.20	14.87	14.27	14.15	13.12	12.42	11.74	11.39	10.67	8.15	1.73	0.70	0.35
1764-165F	–	–	–	14.42	13.7	12.57	10.43†	9.78†	4.66	0.82	1.85	1.13	0.65

in figure 15. Included is a least-absolute-deviation linear fit, which, as expected, shows the increase of absorption with K_s magnitude (as a directly-observable analogue for distance) for both WN and WC stars, as well as a combined plot for all WR stars.

This imaging survey [Paper I, Paper II, and the present paper] has contributed 27 per cent of the currently identified population of Galactic WR stars. The majority of this contribution lies in regions that have not been explored previously in the literature, particularly in magnitude/colour space. Figure 18 shows all currently-known WRs on an NIR colour-magnitude diagram. Before this survey, it might have been believed that such a diagnostic would be effective at isolating candidate WR stars, as the great majority of WRs from the literature are separated from the main field star region. However, when the results from this survey are included, it's clear that Wolf-Rayet stars are found among the

crowded field regions in this diagram, and that this survey is effectively identifying faint, reddened, distant WR stars.

The set of new WR stars and other emission objects presented in this paper is not complete, nor was there any attempt at completeness; the criteria by which we selected WR candidates evolved continuously throughout the follow-up observations. Instead these new WR stars serve as a test for the image subtraction method as a means of identifying new WR stars in the survey images which had already been probed by Papers I and II. These new WR stars are a valuable addition to the catalogue of Galactic WR stars, and measures of completeness will be discussed in the next paper in this series, in preparation.

Table 6. Extinction and distances for confirmed WR stars. It is difficult to differentiate between features of WC4–8; colon (:) indicates an uncertainty of up to ± 2 subtypes. K_s -band extinction was calculated from *2MASS* colours and subtype values provided in Crowther et al. (2006), while M_{K_s} values are derived for spectral subtypes from Rosslove & Crowther (2015). Distances (d) and Galactocentric radii (R_G) are in kpc, with typical uncertainties of ~ 25 per cent.

Name	Subtype	J	H	K_s	$A_{K_s}^{J-K_s}$	$A_{K_s}^{H-K_s}$	A_{K_s}	M_{K_s}	DM	d	R_G
1040-B6C	WN9	13.13	11.90	11.17	1.32	1.32	1.3	-6.32	16.2	17.2	10.7
1089-1117	cLBV/WNL	16.82	12.60	10.28	4.21	4.38	4.3	-6.32	12.3	2.9	6.0
1093-1765	WN6	15.15	12.93	11.57	2.46	2.40	2.4	-4.94	14.1	6.6	3.6
1139-49EA	WC6::	16.25	—	13.09	2.12	—	—	-4.66	—	—	—
1178-66B	WC9	12.49	11.12	10.26	1.57	1.50	1.5	-4.57	13.3	4.6	4.2
1176-B49	WN9h	12.66	11.22	10.41	1.47	1.51	1.5	-6.34	15.3	11.3	3.6
1198-6EC8	WC6::	—	—	13.47	—	—	—	-4.66	—	—	—
1256-1483A	WN9	13.98	12.46	11.86	1.42	1.09	1.26	-6.32	16.9	24.2	15.7
1319-3BC0	WC7:	14.55	—	12.18	—	1.59	—	-4.84	—	—	—
1338-2B3	WN9	12.61	—	8.79	—	2.56	—	-6.32	—	—	—
1343-284	WN8-9	10.47	9.60	9.02	1.06	0.98	1.0	-5.82	13.8	5.8	2.9
1366-438	WN7-8	12.91	—	8.77	—	2.78	—	-5.49	—	—	—
1367-638	WN9	16.15	12.43	10.40	3.70	3.86	3.8	-6.32	12.9	3.9	4.7
1381-19L	WC9	9.66	8.62	8.69	-0.13	0.65	0.3	-4.57	13.0	4.0	7.0
1389-4AB6	WC7	16.13	14.26	12.24	3.69	2.61	3.2	-4.84	13.9	6.1	2.9
1389-1F5D	WN8	—	13.28	11.05	4.05	—	—	-5.82	—	—	—
1446-B1D	WN6	12.21	11.24	10.61	1.14	1.07	1.1	-4.94	14.5	7.8	3.0
1457-673	WC9d	14.52	11.44	9.35	3.81	3.46	3.6	-4.57	10.3	1.1	7.5
1485-6C4	WN6	12.04	10.81	10.02	1.44	1.35	1.4	-4.94	13.6	5.2	4.4
1485-844	WN8	14.72	11.30	9.49	3.29	3.50	3.4	-5.82	12.0	2.4	6.4
1495-1D8A	WC8-9	—	—	11.72	—	—	—	-5.04	—	—	—
1495-705	WN8	14.97	11.38	9.16	4.03	3.89	4.0	-5.82	11.0	1.6	7.1
1514-AA0	WC8	12.92	11.24	10.54	1.29	1.60	1.4	-5.04	14.1	6.7	4.2
1509-2E64	WC9	—	—	12.45	—	—	—	-4.57	—	—	—
1525-2352	WC8:	—	14.75	12.44	4.19	—	—	-5.04	—	—	—
1519-E43	WC7	—	13.04	11.26	3.23	—	—	-4.84	—	—	—
1530-8FA	WN5	12.76	11.43	10.64	1.43	1.42	1.4	-3.86	13.1	4.1	5.4
1541-3C8	WC8	—	13.86	12.15	3.10	—	—	-5.04	—	—	—
1541-197C	WC8	15.14	13.28	11.62	3.03	2.36	2.7	-5.04	14.0	6.2	4.7
1544-FA4	WN5	13.74	—	10.83	1.95	—	—	-3.86	—	—	—
1553-9E8	WN9h	15.76	12.86	10.98	3.44	3.21	3.3	-6.34	14.0	6.3	4.8
1547-1488	WN5	13.96	12.25	11.16	1.99	1.87	1.9	-3.86	13.1	4.1	5.5
1553-15DF	WC8	—	14.80	12.07	4.98	—	—	-5.04	—	—	—
1602-9AF	WN6	13.11	11.62	11.05	1.04	1.38	1.2	-4.94	14.8	9.1	6.1
1603-11AD	WN5	16.13	13.64	12.17	2.69	2.66	2.7	-3.86	13.3	4.7	5.8
1609-1C95	WC9	—	15.07	11.93	5.72	—	—	-4.57	—	—	—
1626-4FC8	[WC6:]	15.59	14.86	13.89	1.77	1.14	1.5	—	—	—	—
1629-14D6	WN9h	14.73	13.44	12.63	1.49	1.41	1.5	-6.34	17.5	31.9	26.4
1627-A6D	WC7::	15.85	13.54	11.75	3.25	2.75	3.0	-4.84	13.6	5.2	5.9
1635-AD8	WN6	15.20	12.87	11.48	2.54	2.49	2.5	-4.94	13.9	6.0	5.9
1653-FFE	WN5-6	15.15	—	11.66	—	2.34	—	-3.86	—	—	—
1651-BB4	WN5	15.83	—	11.73	—	2.74	—	-3.86	—	—	—
1647-1E70	WC8:	—	15.10	12.57	4.60	—	—	-5.04	—	—	—
1659-212	WN9	13.44	10.89	9.53	2.48	2.62	2.6	-6.32	13.3	4.6	6.3
1669-3DF	WN9h	12.79	11.04	9.97	1.95	1.89	1.9	-6.34	14.4	7.5	6.6
1660-1169	WC6:	14.65	13.29	12.08	2.21	1.73	2.0	-4.66	14.8	9.0	7.0
1697-38F	WC9	12.97	—	9.92	2.28	—	—	-4.57	—	—	—
1702-23L	WC8	11.86	11.00	10.21	1.44	1.11	1.3	-5.04	14.0	6.2	6.8
1695-2B7	WC9	13.01	11.09	9.64	2.64	2.26	2.5	-4.57	11.8	2.3	7.3

6 CONCLUSIONS & LOOKING FORWARD

The imaging survey first introduced in Paper I has already produced 27 per cent of the known Galactic WR stars using photometric selection techniques (Shara et al. 2009, 2012). Using new reductions and image-subtraction methods, we have shown in this paper that there are still many more Galactic WR star candidates to be discovered and con-

firmed, particularly in the Southern hemisphere. The Galactic Centre region in particular has not been tapped, as the survey images are so crowded that special care must be taken with them. The pipeline described in this paper is capable of analysing all but the densest regions in our survey.

The WR population simulations presented in Paper I predicted several thousand WR stars in the Milky Way,

Table 7. Lines in the NIR Wolf-Rayet spectrum, a subset of Figer, McLean, & Najarro (1997, table 2). These lines are marked in the spectra shown in figures 6 and 7.

Wavelength (μm)	Transition	Wavelength (μm)	Transition
2.037	He II 15 – 8	2.148	He II 24 – 9
2.059	He I 2s ^1S – 2p $^1\text{P}^0$	2.162	He I 7 ^1L – 4 ^1D
2.071	C IV 3p $^2\text{P}_{1/2}^0$ – 3d $^2\text{D}_{3/2}$	2.165	He II 14 – 8
2.080	C IV 3p $^2\text{P}_{3/2}^0$ – 3d $^2\text{D}_{5/2}$	2.166	H I 7 – 4
2.084	C IV 3p $^2\text{P}_{3/2}^0$ – 3d $^2\text{D}_{3/2}$	2.179	He II 23 – 9
2.097	He II 26 – 9	2.189	He II 10 – 7
2.100	N V 11 – 10	2.217	He II 22 – 9
2.104	C III/N III 8 – 7	2.247	N III 5s $^2\text{S}_{1/2}$ – 5p $^2\text{P}_{3/2}^0$
2.108	C III 5s ^1S – 5p $^1\text{P}^0$	2.278	C IV/N IV 15 – 12
2.113	He I 4s ^3S – 3p ^3P	2.314	He II 20 – 19
2.115	C III/N III 8 – 7	2.320	C IV 13d ^2D – 11p $^2\text{P}^0$
2.116	C III/N III 8 – 7	2.335	C IV 9p $^2\text{P}_{1/2}^0$ – 10d ^2D , 9p $^2\text{P}_{3/2}^0$ – 10d ^2D
2.122	C III 4p $^1\text{P}^0$ – 4d ^1D	2.347	He II 13 – 8
2.139	C IV 9s ^2S – 10p $^2\text{P}^0$	2.379	He II 19 – 9

Table 8. Measured equivalent widths for confirmed WN stars between 2.037 and 2.115 μm . Lines were fit as gaussian profiles using PAN¹ and then summed to find the equivalent width. Atomic transitions for each line are given in table 7. The three numbers in each entry are, in order: line centre from the gaussian fit; equivalent width; line FWHM.

Name	Subtype	He II 2.037 μm	He I 2.059 μm	He II 2.097 μm N V 2.100 μm C III 2.104 μm N III 2.104 μm	C III 2.108 μm He I 2.113 μm C III 2.115 μm N III 2.115 μm
1040-B6C	WN9	–	2.0583 25.21 27.6	–	–
1089-1117	cLBV/WNL	–	2.0581 101.85 20.6	–	2.1127 9.01 28.0
1093-1765	WN6	–	–	–	2.1126 40.27 106.3
1176-B49	WN9h	–	2.0591 61.87 24.7	–	2.1137 7.27 26.2
1256-1438A	WN9	–	2.0592 5.45 24.4	–	–
1338-2B3	WN9	–	2.0554 11.90 29.3	–	–
1343-284	WN8-9	–	2.0549 16.24 42.0	–	–
1366-438	WN7-8	–	2.0540 6.27 16.1	–	–
1367-638	WN9	–	2.0592 57.71 39.0	2.1033 2.72 61.0	2.1138 13.03 37.8
1389-1F5D	WN8	–	2.0601 67.62 55.6	2.1026 1.94 26.0	2.1142 32.98 51.6
1446-B1D	WN6	2.0377 13.76 84.8	2.0638 15.17 108.5	2.0974 2.07 39.6	2.1140 49.41 154.8
1485-6C4	WN6	–	–	2.1060 10.50 44.9	–
1485-844	WN8	–	2.0574 30.01 41.4	–	2.1123 5.15 40.8
1495-705	WN8	–	2.0577 38.48 35.0	–	–
1530-8FA	WN5	2.0385 18.19 87.5	2.0604 2.10 46.0	2.0993 4.19 43.1	2.1145 26.21 131.1
1544-FA4	WN5	2.0356 22.29 118.1	–	–	2.1117 39.51 282.1
1553-9E8	WN9h	–	2.0591 77.32 25.1	–	2.1136 13.25 30.8
1547-1488	WN5	–	–	2.0964 91.42 252.9	2.1095 26.70 68.1
1602-9AF	WN6	–	–	–	2.1069 51.82 182.3
1603-11AD	WN5	2.0373 14.96 87.9	–	2.0923 1.36 43.9	2.1142 23.05 131.8
1629-14D6	WN9h	–	2.0582 14.75 43.9	–	–
1635-AD8	WN6	2.0388 17.52 75.1	2.0611 5.24 43.9	2.0967 5.17 87.9	2.1146 33.55 109.5
1653-FFE	WN5-6	2.0375 19.58 88.0	2.0600 2.97 87.9	2.0961 5.01 65.9	2.1130 27.61 104.8
1651-BB4	WN5	2.0346 13.56 109.9	2.0561 3.53 65.9	–	2.1114 27.17 153.8
1659-212	WN9	–	2.0543 3.81 22.2	–	–
1669-3DF	WN9h	–	2.0579 136.96 31.0	–	2.1124 19.10 30.9

¹ <http://ifs.wikidot.com/pan>

Table 9. Measured equivalent widths for confirmed WN stars between 2.148 and 2.217 μm , using PAN to fit gaussian profiles as in table 8. The three numbers in each entry are, in order: line centre from the gaussian fit; equivalent width; line FWHM.

Name	Subtype	He II 2.148 μm	He I 2.162 μm He II 2.165 μm H I 2.166 μm	He II 2.189 μm	He II 2.217 μm
1040-B6C	WN9	–	2.1655 3.06 9.4	–	–
1089-1117	cLBV/WNL	2.1431 4.0 35.2	–	–	–
1093-1765	WN6	–	2.1633 51.04 107.1	2.1879 49.25 92.4	–
1176-B49	WN9h	–	2.1623 3.57 23.5 2.1663 25.52 27.5	–	–
1256-1438A	WN9	–	2.1671 6.84 24.4	–	–
1338-2B3	WN9	–	2.1637 7.06 45.6	–	–
1343-284	WN8-9	–	2.1628 25.38 57.1	–	–
1366-438	WN7-8	–	2.1628 16.96 52.2	2.1833 4.84 48.9	–
1367-638	WN9	–	2.1657 48.98 49.4	2.1848 1.71 46.7	–
1389-1F5D	WN8	–	2.1648 56.36 76.9	2.1904 6.87 37.0	–
1446-B1D	WN6	2.1471 2.04 62.7	2.1653 60.77 146.8	2.1898 65.02 127.4	2.2165 3.80 89.1
1485-6C4	WN6	–	2.1592 57.82 90.1	2.1834 49.17 87.7	–
1485-844	WN8	–	2.1638 37.66 54.7	–	–
1495-705	WN8	–	2.1640 43.66 45.0	–	2.2057 7.54 42.4
1530-8FA	WN5	2.1485 2.97 71.7	2.1655 33.30 104.3	2.1898 62.55 100.3	–
1544-FA4	WN5	–	2.1643 51.63 219.4	2.1896 123.53 198.4	–
1553-9E8	WN9h	2.1457 9.62 66.9	2.1638 17.09 89.9 2.1664 21.19 20.7	2.1859 6.56 86.8	2.2078 13.22 41.0
1547-1488	WN5	–	2.1627 39.94 88.6	2.1875 120.39 134.6	–
1602-9AF	WN6	–	2.1594 73.61 130.0	2.1881 49.74 103.3	–
1603-11AD	WN5	–	2.1652 36.48 109.9	2.1884 104.70 153.8	–
1629-14D6	WN9h	–	2.1662 16.92 22.0	–	–
1635-AD8	WN6	2.1472 3.81 65.9	2.1651 45.85 100.6	2.1899 54.25 84.5	2.2164 2.35 43.9
1653-FFE	WN5-6	2.1461 3.20 87.9	2.1643 46.18 127.2	2.1884 84.10 122.5	2.2175 5.60 109.9
1651-BB4	WN5	–	2.1631 45.21 138.6	2.1882 121.68 203.4	–
1659-212	WN9	–	2.1636 8.83 46.9	–	–
1669-3DF	WN9h	–	2.1645 57.67 45.7	–	–

which have not yet been identified. However, the results presented here are not inconsistent with those predictions, for a few reasons. First, due to the necessity of spectroscopic follow-up to confirm each WR star, even with a high success rate the number of observations necessary is very large. Second, the majority of WR stars still unidentified lie either on the far side of the Galaxy, and are thus very faint, or near the Galactic Centre in prohibitively crowded fields.

This publication makes use of data products from the Two Micron All Sky Survey, which is a joint project of the University of Massachusetts and the Infrared Processing and Analysis Centre/California Institute of Technology, funded by the National Aeronautics and Space Administration and the National Science Foundation. This publication also makes use of data products from the Wide-field Infrared Survey Explorer, which is a joint project of the University of California, Los Angeles, and the Jet Propulsion Laboratory/California Institute of Technology, funded by the National Aeronautics and Space Administration. AFJM is grateful for financial assistance from NSERC (Canada) and FRQNT (Quebec). This research has made use of the NASA/ IPAC Infrared Science Archive, which is operated by the Jet Propulsion Laboratory, California Institute of Technology, under contract with the National Aeronautics and Space Administration.

GK and MS gratefully acknowledge support from Ethel and Hilary Lipsitz.

REFERENCES

- Acker A., Marcout J., Ochsenbein F., Stenholm B., Tylanda R., Schohn C., European Southern Observatory, Garching (Germany), 1992, 1047 p.
- Crowther P. A., 2007, *ARA&A*, 45, 177
- Crowther P. A., Hadfield L. J., Clark J. S., Negueruela I., Vacca W. D., 2006, *MNRAS*, 372, 1407
- Crowther P. A., Morris P. W., Smith J. D., 2006, *ApJ*, 636, 1033
- Cushing M. C., Vacca W. D., Rayner J. T., 2004, *PASP*, 116, 362
- Detmers R. G., Langer N., Podsiadlowski P., Izzard R. G., 2008, *A&A*, 484, 831
- Evans I. N., et al., 2010, *ApJS*, 189, 37
- Faherty J. K., Shara M. M., Zurek D., Kanarek G., Moffat A. F. J., 2014, *AJ*, 147, 115
- Figer D. F., McLean I. S., Najarro F., 1997, *ApJ*, 486, 420
- Greene T. P., Lada C. J., 1996, *AJ*, 112, 2184
- Guerrero M. A., Chu Y.-H., 2008, *ApJS*, 177, 238
- Gvaramadze V. V., Kniazev A. Y., Fabrika S., 2010, *MNRAS*, 405, 1047
- Hadfield L. J., van Dyk S. D., Morris P. W., Smith J. D., Marston A. P., Peterson D. E., 2007, *MNRAS*, 376, 248
- Indebetouw R., et al., 2005, *ApJ*, 619, 931
- Kerber F., Mignani R. P., Guglielmetti F., Wicenec A., 2003, *A&A*, 408, 1029

A Near-Infrared Survey of the Inner Galactic Plane for Wolf-Rayet Stars III. New Methods: Faintest WR Stars

Table 10. Measured equivalent widths for confirmed WC stars between 2.037 and 2.115 μm , using PAN to fit gaussian profiles as in table 8. The three numbers in each entry are, in order: line centre from the gaussian fit; equivalent width; line FWHM.

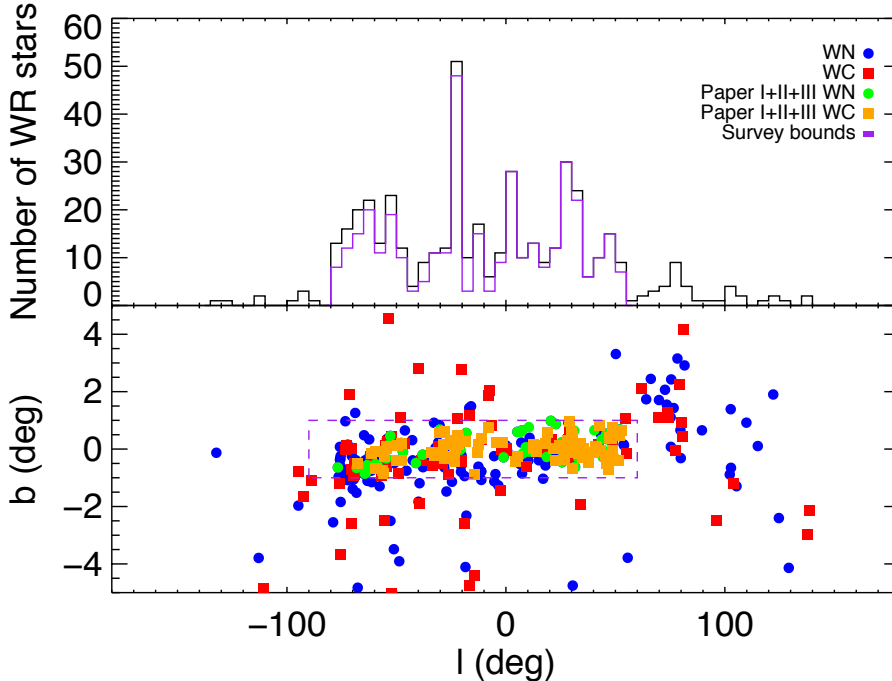
Name	Subtype	He II 2.037 μm	He I 2.059 μm	C IV 2.071 μm C IV 2.080 μm C IV 2.084 μm	C III 2.104 μm C III 2.115 μm
1139-49EA	WC6::	–	–	2.0754 688.74 203.1	2.1116 105.67 159.2
1178-66B	WC9	–	2.0603 76.96 73.1	2.0786 6.38 41.3 2.0854 7.74 55.8	2.1086 12.00 55.0 2.1141 28.18 54.6
1198-6EC8	WC6::	–	–	2.0751 1856.57 267.1	2.1132 269.48 207.5
1319-3BC0	WC7:	–	–	2.0750 595.53 241.5	2.1123 110.36 237.8
1381-19L	WC9	–	2.0553 88.10 63.3	2.0693 170.15 193.5	2.1068 123.28 224.5
1389-4AB6	WC7	–	–	2.0767 309.24 244.1	2.1164 61.56 170.9
1457-673 ^a	WC9d	–	2.0536 21.86 55.3	–	–
1495-1D8A	WC8-9	–	2.0590 92.39 98.7	2.0793 78.20 114.0	2.1109 114.26 91.9
1514-AA0	WC8	–	–	2.0765 339.28 191.6	2.1129 131.97 145.3
1509-2E64	WC9	2.0385 6.25 46.7	2.0622 196.58 130.6	2.0807 153.45 131.8	2.1131 166.77 123.0
1525-2352	WC8:	–	–	2.0779 390.00 175.8	2.1136 119.99 109.9
1519-E43	WC7	–	–	2.0755 448.47 213.1	2.1115 178.18 161.9
1541-3C8	WC8	–	–	2.0822 217.71 145.9	2.1159 177.26 151.7
1541-197C ^b	WC8	–	–	2.0723 270.80 188.4	2.1087 157.25 155.7
1553-15DF	WC8	–	–	2.0692 33.69 100.5 2.0800 55.07 104.4	2.1125 41.06 115.7
1609-1C95	WC9	–	2.0604 46.12 80.4	2.0694 6.09 34.2 2.0785 12.22 48.5 2.0851 11.35 59.6	2.1126 39.84 93.2
1626-4FC8	[WC6:]	–	–	2.0696 94.76 65.9 2.0798 353.35 109.9	2.1142 114.74 109.9
1627-A6D	WC7::	–	–	2.0760 693.81 250.4	2.1131 171.41 282.6
1647-1E70	WC8:	–	–	2.0764 605.00 192.3	2.1123 163.74 131.8
1660-1169	WC6:	–	–	2.0713 1059.04 179.9 2.0857 373.04 126.7	2.1107 309.08 283.3
1697-38F	WC9	2.0387 3.48 89.8	2.0614 12.69 82.2	2.0683 10.22 48.4 2.0799 62.47 139.0	2.1122 61.58 113.5
1702-23L	WC8	–	–	2.0761 678.75 204.2	2.1114 575.71 163.1
1695-2B7 ^c	WC9	2.0383 4.12 71.2	2.0626 14.67 83.4	2.0687 19.80 50.0 2.0799 106.61 128.7	2.1126 91.34 113.1

Lépine S., Moffat A. F. J., 1999, ApJ, 514, 909
Lançon A., Hauschildt P. H., Ladjal D., Mouhcine M., 2007, A&A, 468, 205
Lançon A., Wood P. R., 2000, A&AS, 146, 217
Landsman W. B., 1993, ASPC, 52, 246
Lang D., Hogg D. W., Mierle K., Blanton M., Roweis S., 2010, AJ, 139, 1782
Mauerhan J. C., Munro M. P., Morris M. R., Stolovy S. R., Cotera A., 2010, ApJ, 710, 706
Mauerhan J., Van Dyk S., Morris P., 2009, AAS, 214, #605.09
Mauerhan J. C., Van Dyk S. D., Morris P. W., 2011, AJ, 142, 40
Messineo M., Menten K. M., Churchwell E., Habing H., 2012, A&A, 537, AA10
Miszalski B., Parker Q. A., Acker A., Birkby J. L., Frew D. J., Kovacevic A., 2008, MNRAS, 384, 525
Predehl P., Schmitt J. H. M. M., 1995, A&A, 293, 889
Rayner J. T., Cushing M. C., Vacca W. D., 2009, ApJS, 185, 289
Rieke G. H., Lebofsky M. J., 1985, ApJ, 288, 618
Rosslowe C. K., Crowther P. A., 2015, MNRAS, 447, 2322
Shara M. M., Moffat A. F. J., Smith L. F., Niemela V. S., Potter M., Lamontagne R., 1999, AJ, 118, 390

Shara M. M., et al., 2009, AJ, 138, 402 (Paper I)
Shara M. M., Faherty J. K., Zurek D., Moffat A. F. J., Gerke J., Doyon R., Artigau E., Drissen L., 2012, AJ, 143, 149 (Paper II)
Skinner S., Güdel M., Schmutz W., Zhekov S., 2006, Ap&SS, 304, 97
Skrutskie M. F., et al., 2006, AJ, 131, 1163
Smith J. D. T., Cushing M., Barletta A., McCarthy D., Kulesa C., Van Dyk S. D., 2012, AJ, 144, 166
Stetson P. B., 1987, PASP, 99, 191
Stetson P. B., 1994, PASP, 106, 250
Stringfellow G. S., Gvaramadze V. V., Beletsky Y., Kniazev A. Y., 2012, IAUS, 282, 267
Urquhart J. S., et al., 2009, A&A, 501, 539
Vacca W. D., Cushing M. C., Rayner J. T., 2004, PASP, 116, 352
van der Hucht K. A., 2006, A&A, 458, 453
van der Hucht K. A., 2001, yCat, 3215, 0
Wachter S., Mauerhan J., van Dyk S., Hoard D. W., Morris P., 2011, BSRSL, 80, 291
Wolf C. J. E., Rayet G., 1867, Comptes Rendus, 65, 292
Woosley S. E., Bloom J. S., 2006, ARA&A, 44, 507
Wright E. L., et al., 2010, AJ, 140, 1868

Table 11. Measured equivalent widths for confirmed WC stars between 2.139 and 2.217 μm , using PAN to fit gaussian profiles as in table 8. The three numbers in each entry are, in order: line centre from the gaussian fit; equivalent width; line FWHM.

Name	Subtype	C IV 2.139 μm	He I 2.162 μm He II 2.165 μm	He II 2.189 μm	He II 2.217 μm
1139-49EA	WC6::	–	–	2.1896 33.45 95.5	–
1178-66B	WC9	2.1392 0.98 26.8	2.1643 32.19 80.3	–	–
1198-6EC8	WC6::	–	–	2.1880 54.71 134.3	–
1319-3BC0	WC7:	–	2.1687 28.39 170.2	2.1890 43.11 155.7	–
1381-19L	WC9	–	2.1646 40.83 117.9	2.1867 43.35 160.5	2.2189 61.83 156.4
1389-4AB6	WC7	–	2.1575 3.23 51.2	2.1842 29.36 170.9	–
1457-673 ^a	WC9d	–	2.1625 21.57 65.2	–	–
1495-1D8A	WC8-9	2.1366 11.39 39.0	2.1616 60.14 66.2	2.1829 32.05 152.2	–
1514-AA0	WC8	2.1405 8.23 87.9	2.1648 58.78 148.9	2.1889 51.93 117.5	–
1509-2E64	WC9	2.1397 14.98 109.9	2.1647 59.88 117.9	2.1879 44.72 115.0	2.2230 10.25 109.9
1525-2352	WC8:	2.1374 3.58 65.9	2.1700 6.90 65.9	2.1897 21.92 109.9	–
1519-E43	WC7	–	2.1628 96.08 181.4	2.1876 70.14 143.9	–
1541-3C8	WC8	–	–	2.1925 34.46 113.8	2.2147 96.09 282.5
1541-197C ^b	WC8	2.1318 44.09 154.9	2.1637 11.95 61.6	2.1865 8.98 70.7	–
1553-15DF	WC8	–	2.1648 12.28 93.3	2.1859 14.98 130.2	–
1609-1C95	WC9	–	2.1646 11.22 67.7	2.1841 15.61 132.3	–
1626-4FC8	[WC6:]	–	2.1661 16.61 43.9	2.1900 49.48 87.9	–
1627-A6D	WC7::	–	2.1591 19.65 144.7	2.1850 82.65 267.4	–
1647-1E70	WC8:	2.1362 5.07 65.9	2.1670 15.77 87.9	2.1887 32.37 109.9	–
1660-1169	WC6:	–	–	2.1855 60.61 219.5	–
1697-38F	WC9	2.1396 6.78 87.9	2.1638 17.12 106.4	2.1881 11.09 78.8	2.2231 2.63 68.9
1702-23L	WC8	–	2.1617 251.42 94.9	2.1848 958.74 302.8	–
1695-2B7 ^c	WC9	2.1394 6.73 65.0	2.1641 21.24 97.2	2.1894 12.09 62.8	–

^a This spectrum also contains the C III line at 2.122 μm (2.1264 4.18 29.0).^b This spectrum also contains the He II line at 2.148 μm (2.1501 29.00 108.7).^c This spectrum also contains the He II line at 2.179 μm (2.1822 11.86 97.0).**Figure 13.** Top: A histogram of WR stars per 5° of longitude, with those WRs lying within the survey bounds overplotted in cyan. 80 per cent of all current WR stars lie within the bounds of the survey. The histogram shows clear spikes where the telescope looks along the Milky Way’s spiral arms, as predicted by simulations presented in the appendix of Paper I. Bottom: The distribution of WR stars projected on the sky, as a function of Galactic latitude and longitude. Blue circles (WN) and red squares (WC) are WR stars from the literature, while green circles (WN) and orange squares (WC) indicate the contribution by this survey, as detailed in Papers I, II, and this work. The cyan box shows the survey extent; the great majority of WR stars in the Galaxy lie in the Galactic plane, within 60–90° of the Galactic centre.

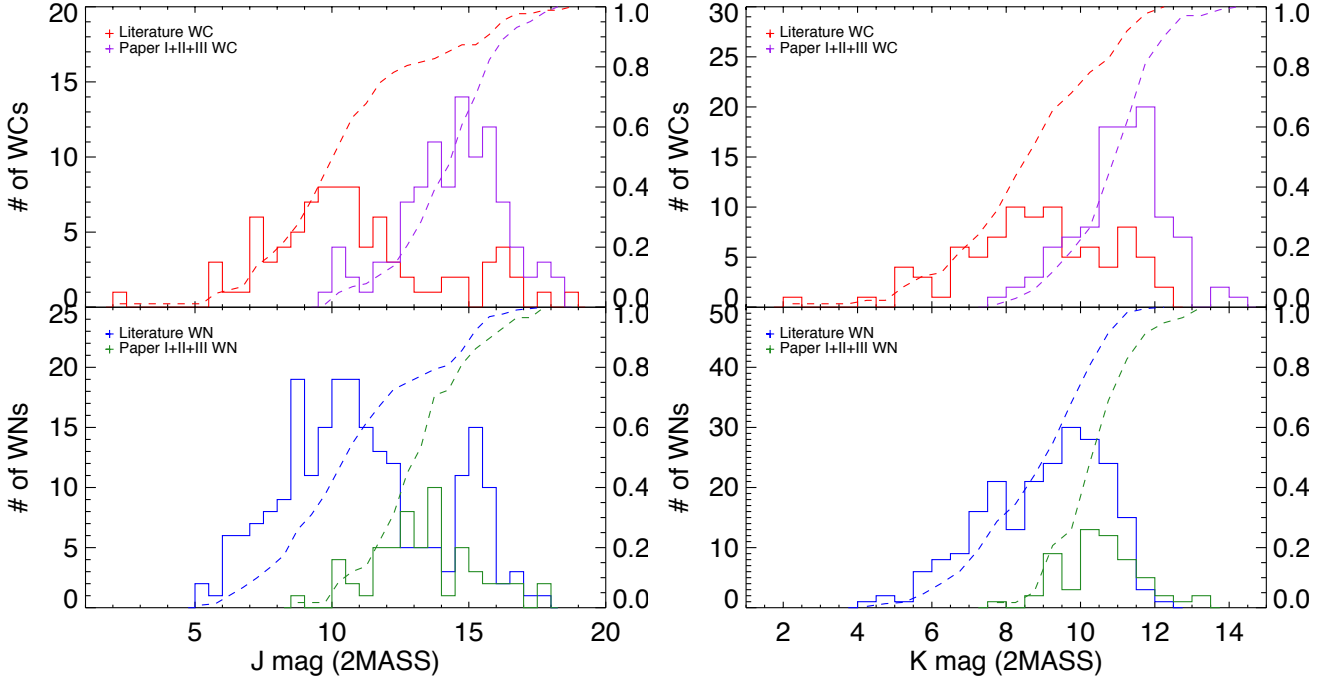


Figure 14. Histogram of J -band (left) and K -band (right) $2MASS$ magnitudes for WN and WC stars, identified in the literature or from the Shara et al. survey. Also shown is the cumulative fraction identified, as a function of magnitude in each case. The survey detailed in Papers I and II and in this paper has contributed WR stars in regions of magnitude-space which are poorly probed by the literature; the survey has identified far more faint WCs in particular than other surveys.

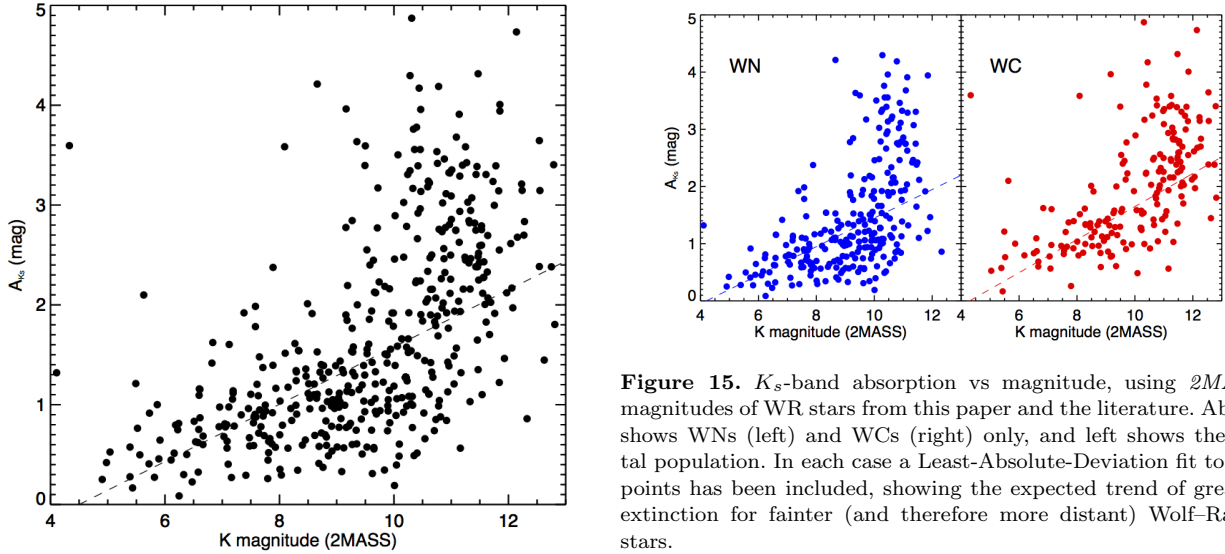


Figure 15. K_s -band absorption vs magnitude, using $2MASS$ magnitudes of WR stars from this paper and the literature. Above shows WNs (left) and WCs (right) only, and left shows the total population. In each case a Least-Absolute-Deviation fit to the points has been included, showing the expected trend of greater extinction for fainter (and therefore more distant) Wolf-Rayet stars.

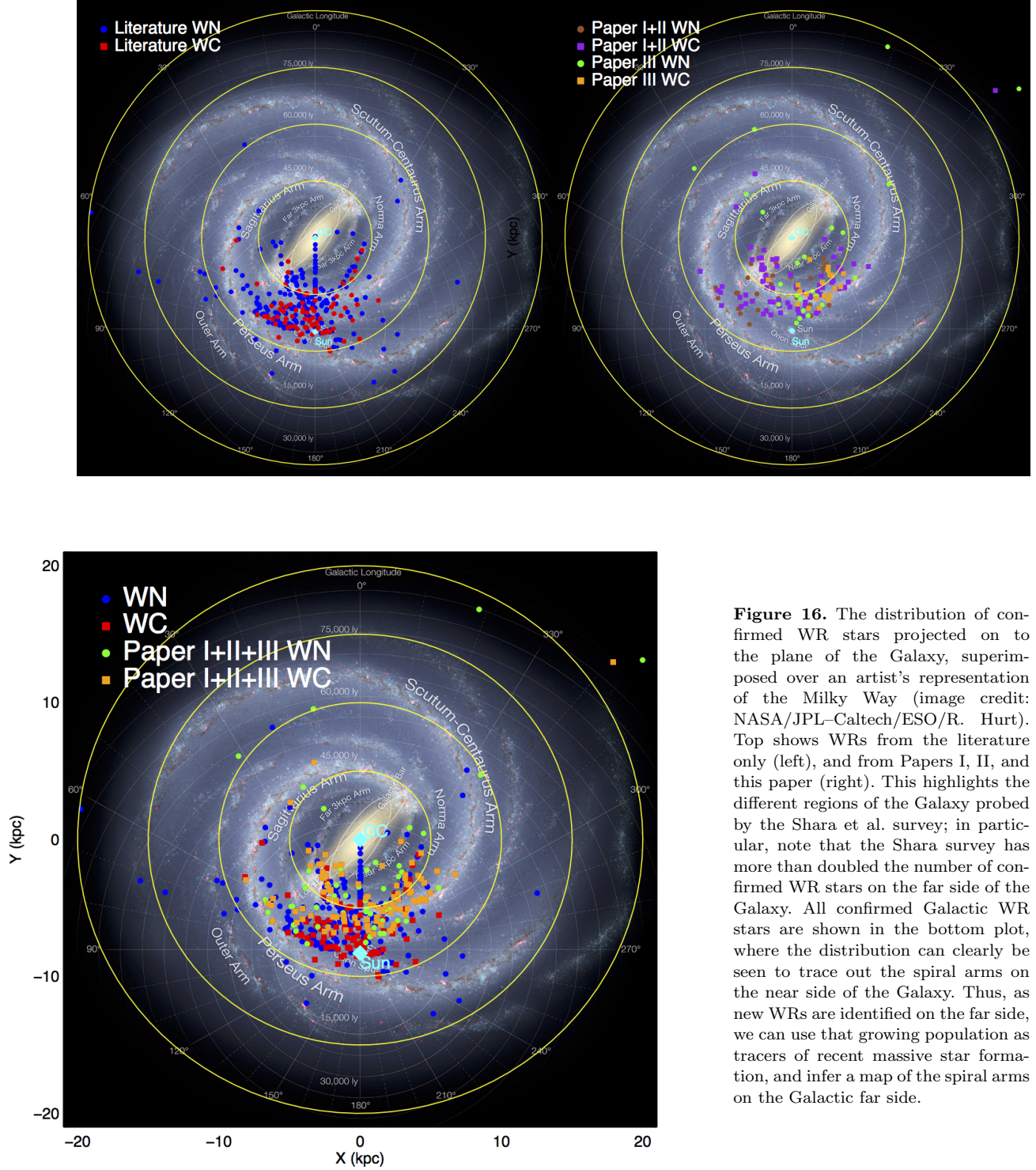


Figure 16. The distribution of confirmed WR stars projected on to the plane of the Galaxy, superimposed over an artist’s representation of the Milky Way (image credit: NASA/JPL–Caltech/ESO/R. Hurt). Top shows WRs from the literature only (left), and from Papers I, II, and this paper (right). This highlights the different regions of the Galaxy probed by the Shara et al. survey; in particular, note that the Shara survey has more than doubled the number of confirmed WR stars on the far side of the Galaxy. All confirmed Galactic WR stars are shown in the bottom plot, where the distribution can clearly be seen to trace out the spiral arms on the near side of the Galaxy. Thus, as new WRs are identified on the far side, we can use that growing population as tracers of recent massive star formation, and infer a map of the spiral arms on the Galactic far side.

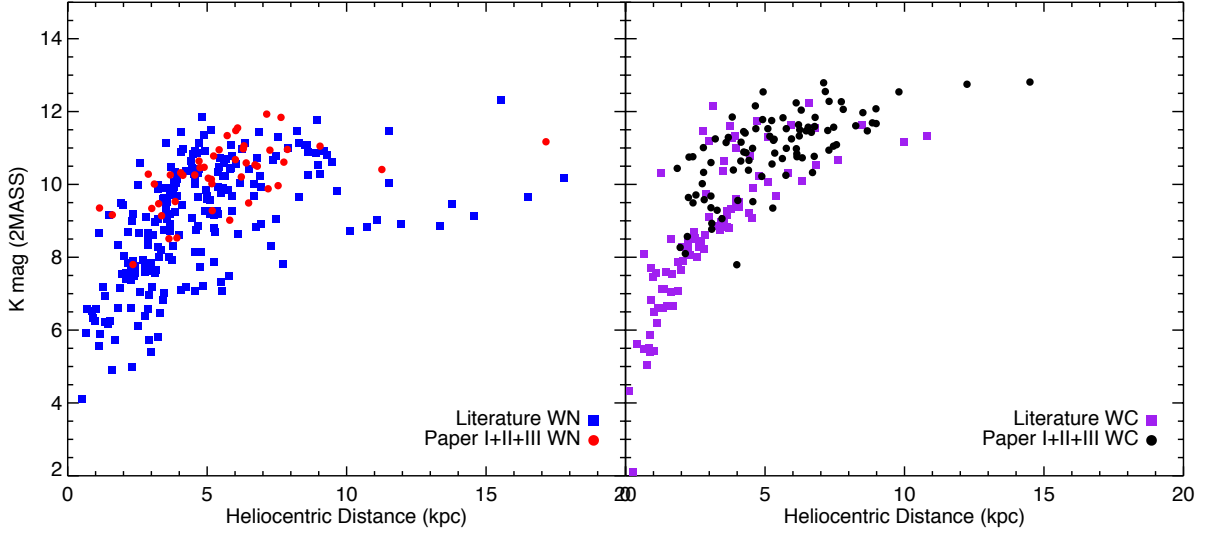


Figure 17. K_s -band magnitude ($2MASS$) as a function of heliocentric distance for WCs and WNs. The Shara et al. survey has identified the most distant and the faintest WNs and (especially) WCs in the Milky Way.

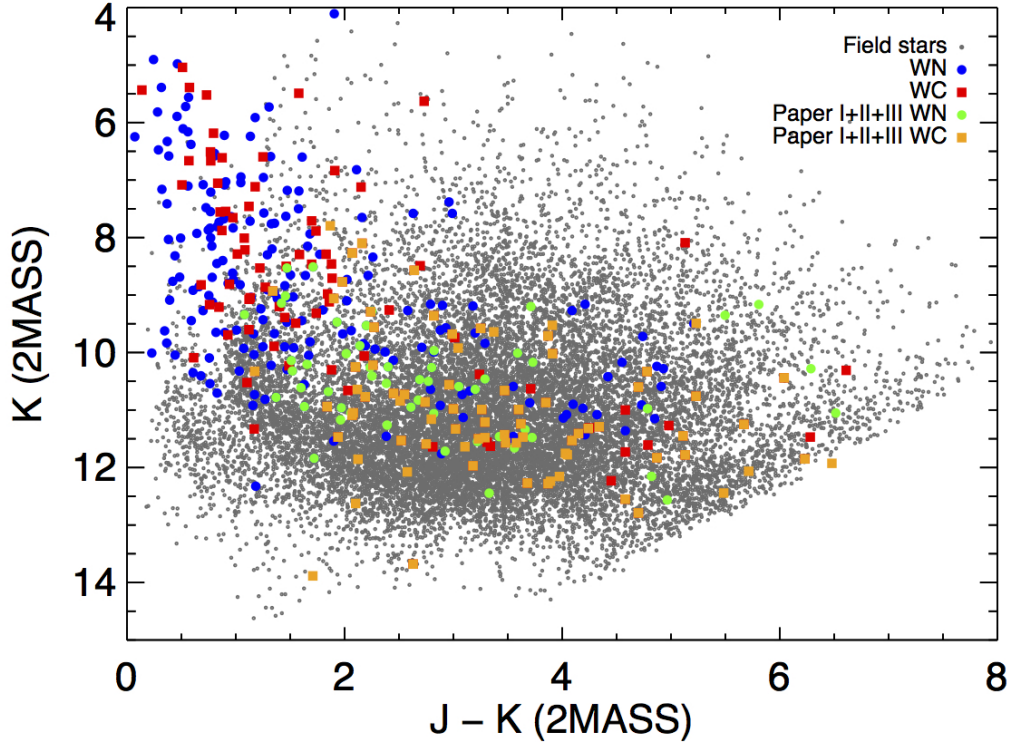


Figure 18. NIR colour-magnitude diagram, using $2MASS$ magnitudes of field and WR stars. This diagram demonstrates that the Shara et al survey is probing a more distant population of WRs than previous methods. The WRs we have identified are significantly fainter and redder than those in the literature, and would have been lost among the field stars by other selection methods.

APPENDIX A: FINDER CHARTS FOR CONFIRMED WR STARS

Included here are the first 9 finder charts for confirmed WR stars discussed in this paper, taken from the Shara et al. J and CONT2 (as an analogue for *2MASS* K_s) survey images. The remainder of the finder charts are available as supplementary online-only data.

